Supporting information

Coordination-Assembly of a Redox-Active Pd_6L_3 Cage for Aerobic C(sp^3)–H Bond Photooxidation of Aromatic Cyclic Ethers

Yu-Hang Hu,[ab] Fan Yin,[bc] Shun-Xing Hong,[ab] Li-Peng Zhou,[bc] Ke-Han Tang,[b] Ying-Mei Zhong,[bc] Chen-Chen Li,[bc] Li-Xuan Cai*[abc] and Qing-Fu Sun*[abc]

---

[a] *College of Chemistry and Materials Science, Fujian Normal University, Fuzhou 350007, PR China.*

[b] *Fujian College, University of Chinese Academy of Sciences, Fuzhou 350002, PR China. E-mail: lxcai@fjirsm.ac.cn, qfsun@fjirsm.ac.cn.*

[c] *University of Chinese Academy of Sciences, Beijing, 100049, PR China.*

Supplementary Information available: Experimental details, NMR data, ESI-MS data, supplemental Figures and Tables. CCDC 2417620. For ESI and crystallographic data in CIF. See DOI: 10.1039/x0xx00000x

Content

1. Materials and methods

2,4,6-tris(4-pyridyl)-1,3,5-triazine (4-TPT) and 4,4'''-bis(bromomethyl)-1,1':4',1'':4'',1'''-quaterphenyl were synthesized as reported previously in the literature.[S1,S2] The compound 2,4,6-trimethyl-1,3,5-triazine and p-quaterphenyl were commercially obtained, while (N,N′,N″-trimethyl-2,4,6-tris(4-pyridyl)-1,3,5-triazine tris(hexafluorophosphate) ($Me_3TPT\cdot(PF_6)_3$) was synthesized as reported previously in the literature.[S3] Deuterated solvents were purchased from Admas, Sigma-Aldrich and J&K scientific. The NMR chemical shifts (δ) are reported in ppm (parts per million) and were determined with respect to solvent signal originated due to incomplete deuteration of the solvents ($\delta = 4.79$ for D_2O, $\delta = 2.50$ for DMSO-d_6, $\delta = 7.26$ for $CDCl_3$ in ^1H NMR). Cyclic voltammetry (CV) experiments were carried out in argon-purged solutions of DMSO with 0.1 M tetra(nbutyl)ammonium hexa-fluorophosphate ($TBAPF_6$) as electrolyte at a scan rate of 100 mV/s at room temperature. A glassy carbon was used as working electrode, Ag/AgCl as the reference electrode, and Pt wire as the counter electrode.

2. Single crystal X-ray diffraction studies

X-ray diffraction study for cage **1** was carried out on micro-focus metaljet diffractometer using Ga Kα radiation ($\lambda = 1.3405$ Å). Data reduction was performed with the CrysAlisPro package.[S4]The structures were solved by direct methods and refined by full-matrix least-squares on F^2 with anisotropic displacement using the SHELX software package.[S5] In this case, solvent molecules and Partial anions were highly disordered and could not be reasonably located. These residual intensities were removed by PLATON/SQUEEZE routine.[S6]

Crystal data for **1**: Space group $P6_3/mmc$, a = 25.0141(9) Å , b = 25.0141(9) Å, c = 60.039(4) Å, 32534(3) $Å^3$, Z = 2, T = 275(2) K. Anisotropic least-squares refinement on 4078 independent merged reflections ($R_{int} = 0.0557$), converged at residual $wR_2 = 0.4294$for all data; residual $R_1 = 0.1249$ for 1753 observed data [$I > 2\sigma(I)$], and goodness of fit (GOF) = 1.379. (CCDC: 2417620)

Note: One alert level A error and two alert level B errors were found through the IUCR's CheckCIF routine for the data of **1**. These alerts all result from the limited diffraction ability of this giant supramolecular assembly in the crystal state.

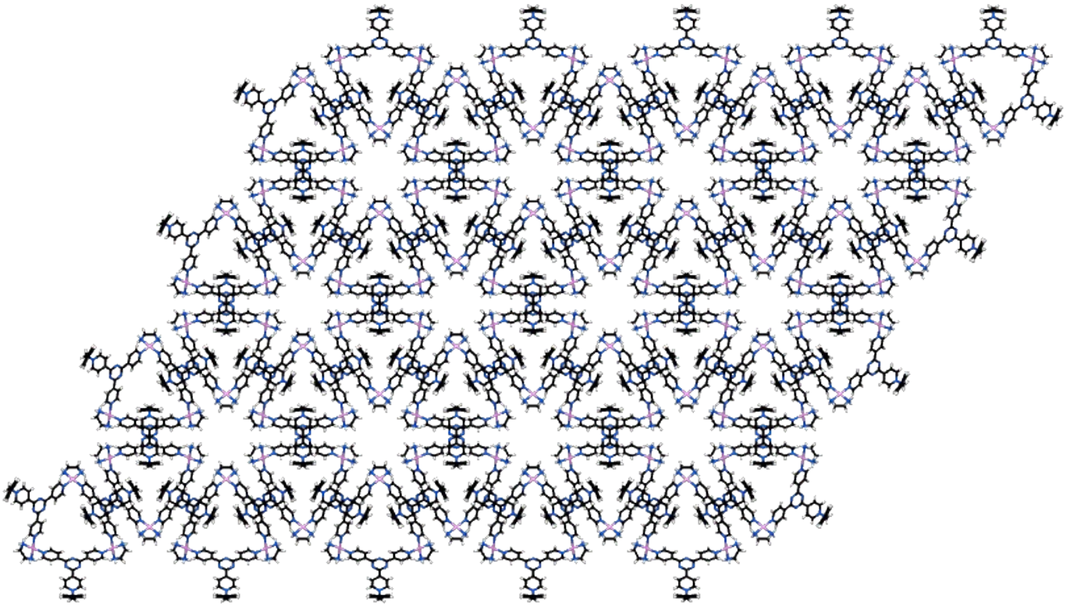

Figure S1. Crystal packing viewed along c axis, showing 3D hierarchical structure through face-to-face π-π stacking interaction between TPT panels.

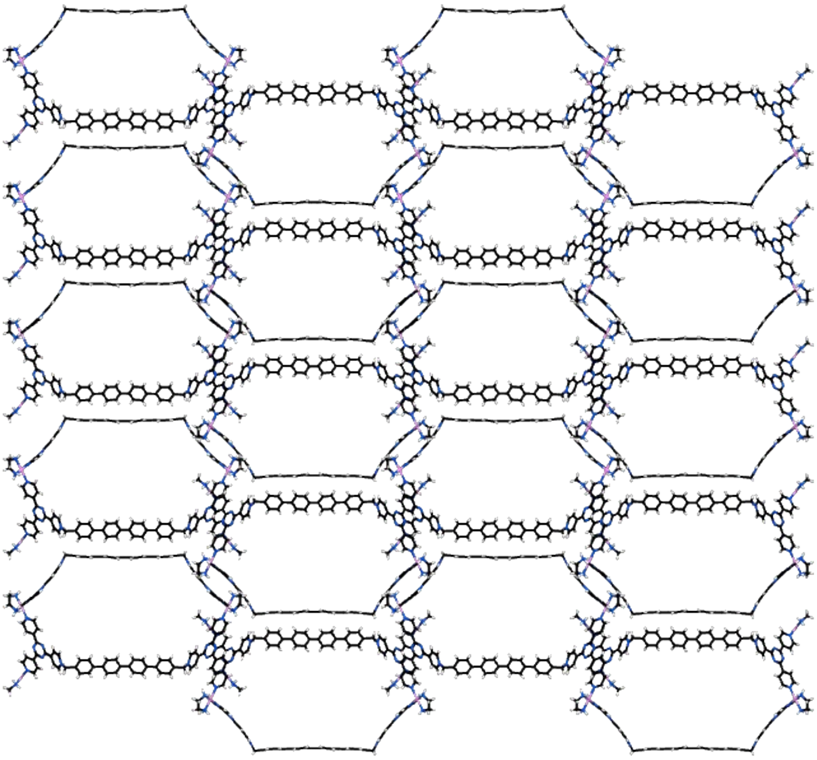

Figure S2. Crystal packing viewed along b axis, showing 3D hierarchical structure through face-to-face π-π stacking interaction between TPT panels.

Table S1. Crystal data and structure refinement for cage **1**.

Identification code	hyh-2_sq	
Empirical formula	C198 H180 F0 N48 P0 Pd6	
Formula weight	3870.29	
Temperature	275(2) K	
Wavelength	1.3405 Å	
Crystal system	Hexagonal	
Space group	$P6_3/mmc$	
Unit cell dimensions	a = 25.0141(9) Å	α= 90°.
	b = 25.0141(9) Å	β= 90°.
	c = 60.039(4) Å	γ = 120°.
Volume	32534(3) Å^3	
Z	2	
Density (calculated)	0.395 Mg/m^3	
Absorption coefficient	0.986 mm^{-1}	
F(000)	3960	
Crystal size	0.20 x 0.15 x 0.13 mm^3	
Theta range for data collection	1.773 to 35.644°.	
Index ranges	-20<=h<=21, -17<=k<=20, -29<=l<=50	
Reflections collected	30958	
Independent reflections	4078 [R(int) = 0.0557]	
Completeness to theta = 35.644°	97.3 %	
Refinement method	Full-matrix least-squares on F^2	
Data / restraints / parameters	4078 / 172 / 193	
Goodness-of-fit on F^2	1.379	
Final R indices [I>2sigma(I)]	R1 = 0.1249, wR2 = 0.3844	
R indices (all data)	R1 = 0.1867, wR2 = 0.4294	
Extinction coefficient	n/a	
Largest diff. peak and hole	0.598 and -0.384 e.Å^{-3}	

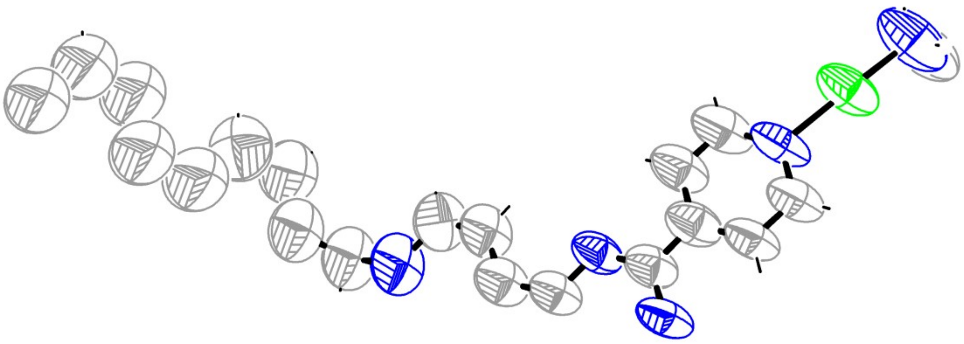

Figure S3. Ortep drawing of the asymmetric unit in the crystal structure of cage **1** at 30% probability level.

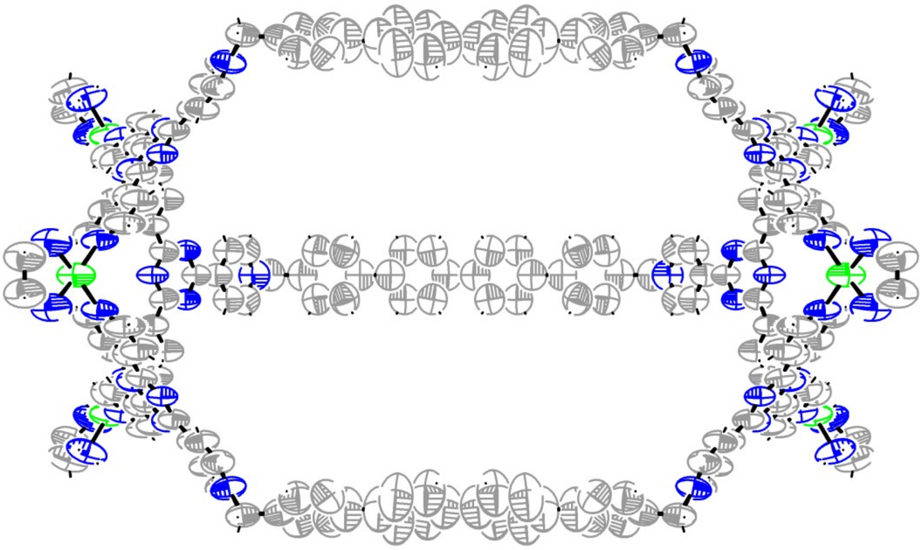

Figure S4. Ortep drawing of cage of cage **1** at 30% probability level.

3. Supplemental Figures and tables

3.1 Synthesis of ligand L and Bz-TPT$^+$

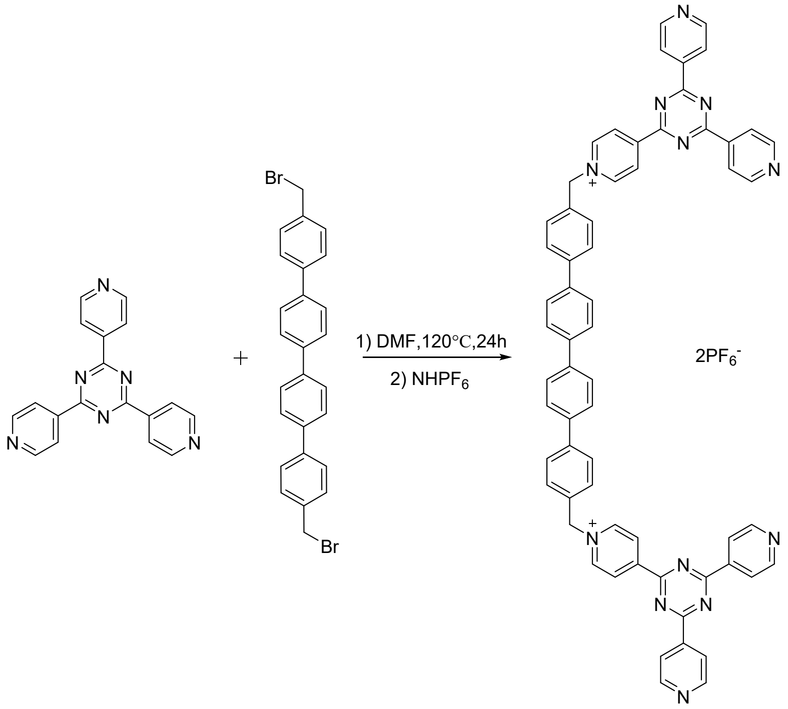

Scheme S1. Synthesis of ligand **L**·$(PF_6)_2$.

Synthesis of Ligand L: Under a N_2 atmosphere, 2,4,6-tris(4-pyridyl)-1,3,5-triazine (4-TPT, 201 mg, 0.647 mmol) was added to anhydrous *N,N*-dimethylformamide (DMF, 100 mL) and stirred at 120 °C until a clear solution was obtained. Subsequently, 4,4'''-bis(bromomethyl)-1,1':4',1'':4'',1'''-quaterphenyl (91 mg, 0.185 mmol) was suspended in DMF (15 mL), thoroughly purged with nitrogen, and slowly added dropwise to the above solution. The mixture was stirred at 120 °C for 24 hours, yielding a green precipitate. The precipitate was filtered, and washed with ethanol. The filter cake was then dissolved in hot water by adding a HNO_3 solution (1 M, 10 mL), followed by counterion exchange of excess sodium tetrafluoroborate ($NaBF_4$). The final product, L·$(BF_4)_2$ (M = 1131.12 g/mol, 110 mg, 53% yield), was collected by filtration. Similarly, L·$(PF_6)_2$ were obtained by counterion exchange with ammonium hexafluorophosphate (NH_4PF_6). For L·$(BF_4)_2$, ^{1}H NMR (400 MHz, DMSO-*d*$_6$, 298 K) δ 9.57 (d, *J* = 6.4 Hz, 2H), 9.42 (d, *J* = 6.4 Hz, 2H), 9.03 (d, *J* = 5.6 Hz, 4H), 8.79 (d, *J* = 5.6 Hz, 4H), 7.88 – 7.84 (m, 6H), 7.74 (d, *J* = 8.0 Hz, 2H), 6.10 (s, 2H). ^{13}C NMR (101 MHz, DMSO-*d*$_6$, 298K) δ 171.39, 168.61, 150.61, 150.38, 146.79, 143.14, 141.05, 139.36, 138.77, 133.93, 130.04, 127.86, 127.73, 127.67, 123.30, 63.81. For L·$(PF_6)_2$: ^{1}H NMR (400 MHz, DMSO-*d*$_6$, 298 K) δ 9.56 (d, *J* = 6.0 Hz, 2H), 9.40 (d, *J* = 6.0 Hz, 2H), 8.99 (d, *J* = 5.2 Hz, 4H), 8.71 (d, *J* = 5.2 Hz, 4H), 7.88 – 7.84 (m, 6H), 7.73 (d, *J* = 7.6 Hz, 2H), 6.10 (s, 2H). ESI-TOF-MS: m/z calcd for $[L^2(PF_6^-)]^{1+}$ 1101.3438 found 1101.3448; m/z calcd for $[L^2]^{2+}$ 478.1900 found 478.1883.

Synthesis of Ligand Bz-TPT$^+$: Under N_2 atmosphere, 2,4,6-tris (4-pyridyl) -1,3,5-triazine (4-TPT, 400 mg, 1.28 mmol) was added to anhydrous DMF (100 mL) and stirred at 120 °C until a clear solution was obtained. The solution was treated dropwise with benzyl bromide (72.97 mg, 0.427 mmol) dissolved in DMF (10 mL), and maintained at 120 °C for 24 hours to form an orange transparent solution. After cooling, filtering, and drying, the filter cake was dissolved in hot water at 80 °C by adding of HNO_3 solution (1 M, 2 mL) and precipitated out by excess ammonium hexafluorophosphate (NH_4PF_6). The resulting product was collected by filtration, washed with water, and dried to obtain a white solid of pure **Bz-TPT**·(PF_6) (M=548.46 g/mol, 125mg, yield of 53%). ^{1}H NMR (400 MHz, DMSO-*d*$_6$) δ 9.51 (d, *J* = 6.4 Hz, 2H), 9.40 (d, *J* = 6.4 Hz, 2H), 9.03 (d, *J* = 5.4 Hz, 4H), 8.79 (d, *J* = 5.4 Hz, 4H), 7.60 (d, *J* = 7.0 Hz, 2H), 7.49 (d, *J* = 7.4 Hz, 3H), 6.04 (s, 2H). ^{13}C NMR (101 MHz, DMSO-*d*$_6$) δ 170.38, 168.97, 147.02, 146.83, 134.66, 133.60, 129.99, 129.81, 129.46, 129.25, 127.78, 125.17, 64.17.

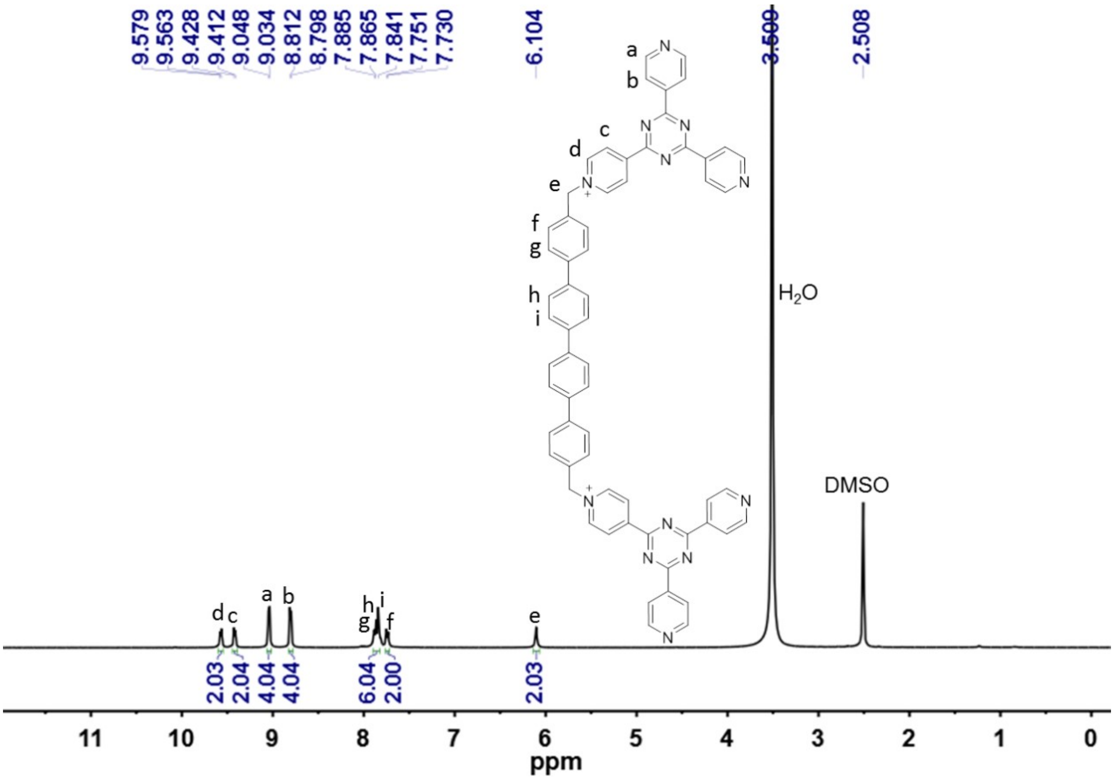

Figure S5. ^{1}H NMR spectrum (400 MHz, DMSO-*d*$_6$, 298 K) of **L**·$(BF_4)_2$.

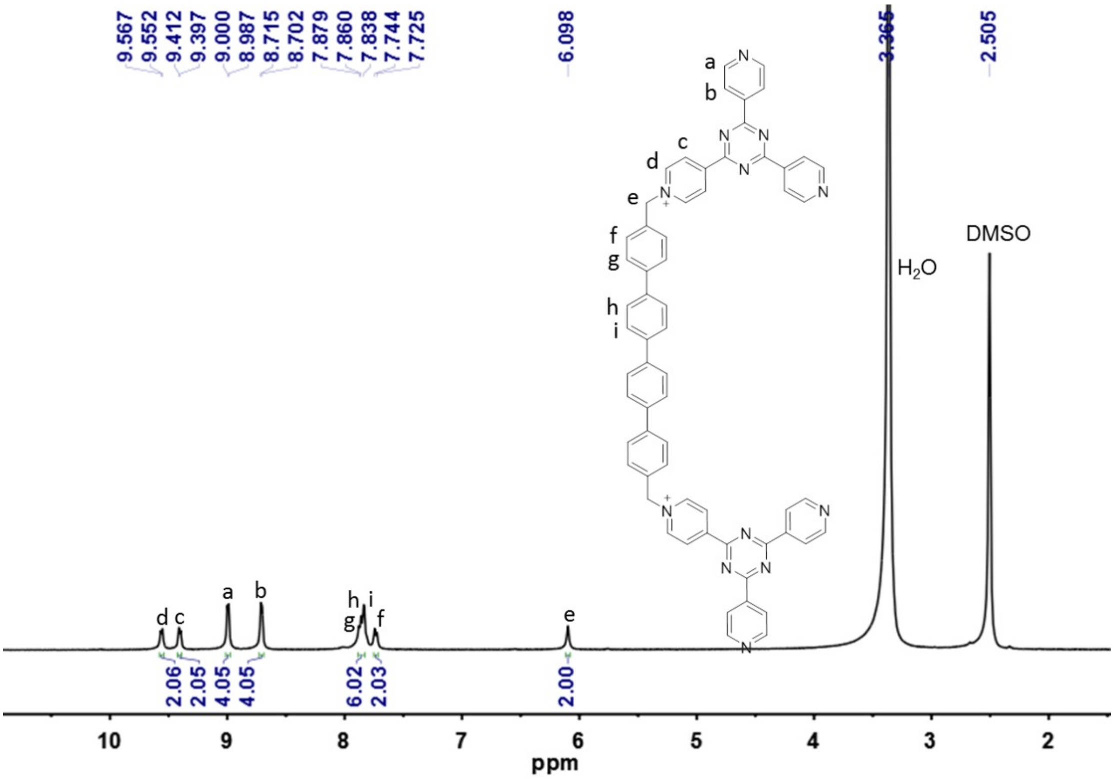

Figure S6. ^{1}H NMR spectrum (400 MHz, DMSO-*d*$_6$, 298 K) of **L·(PF$_6$)$_2$**.

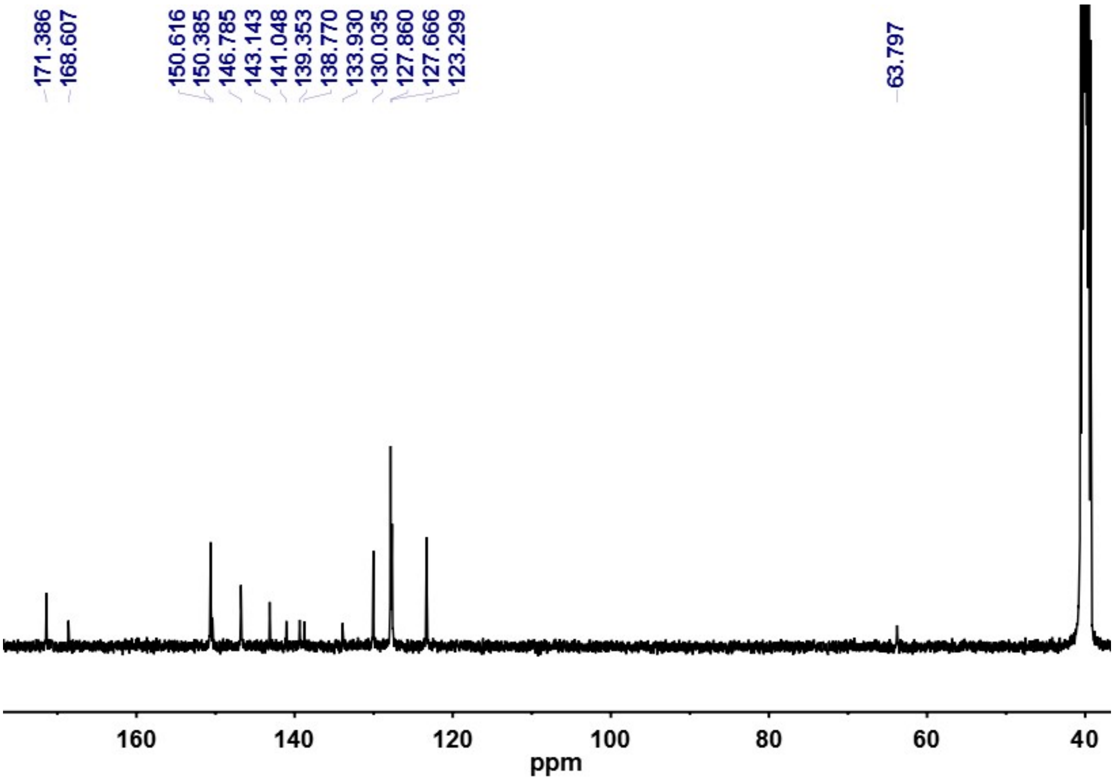

Figure S7. ^{13}C NMR spectrum (101 MHz, DMSO-*d*$_6$, 298 K) of **L·(PF$_6$)$_2$**.

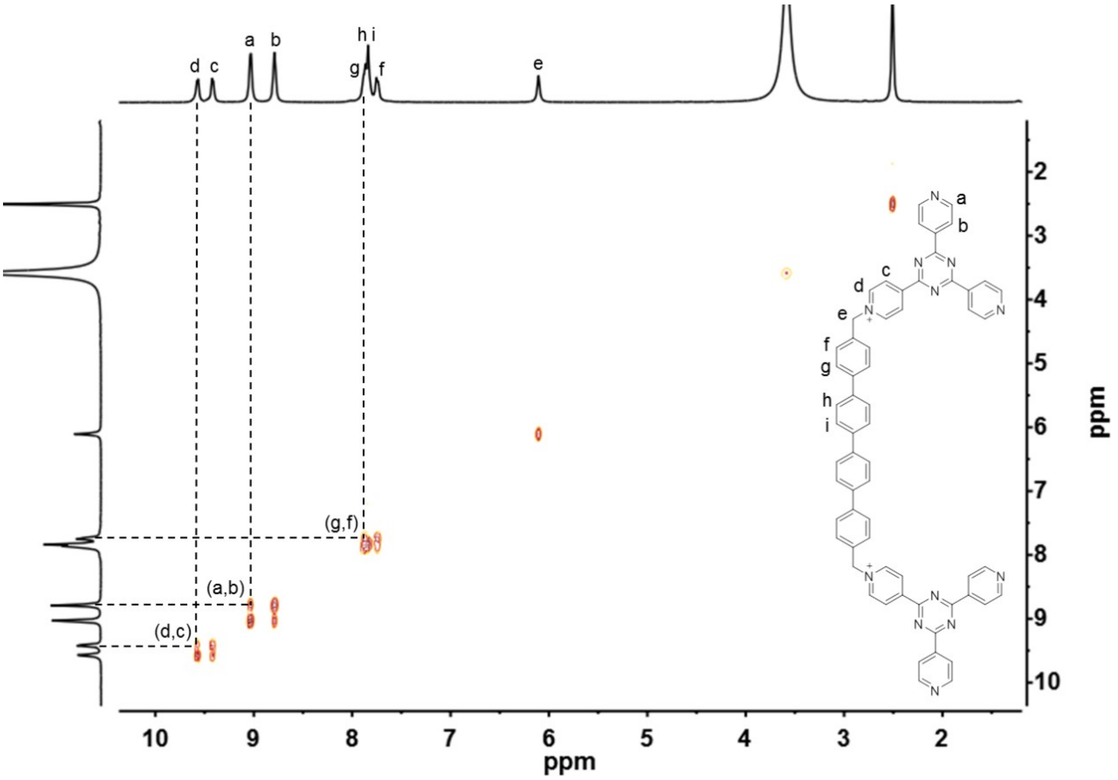

Figure S8. ^{1}H-^{1}H COSY NMR spectrum (400 MHz, DMSO-d_6, 298 K) of **L·(PF$_6$)$_2$**.

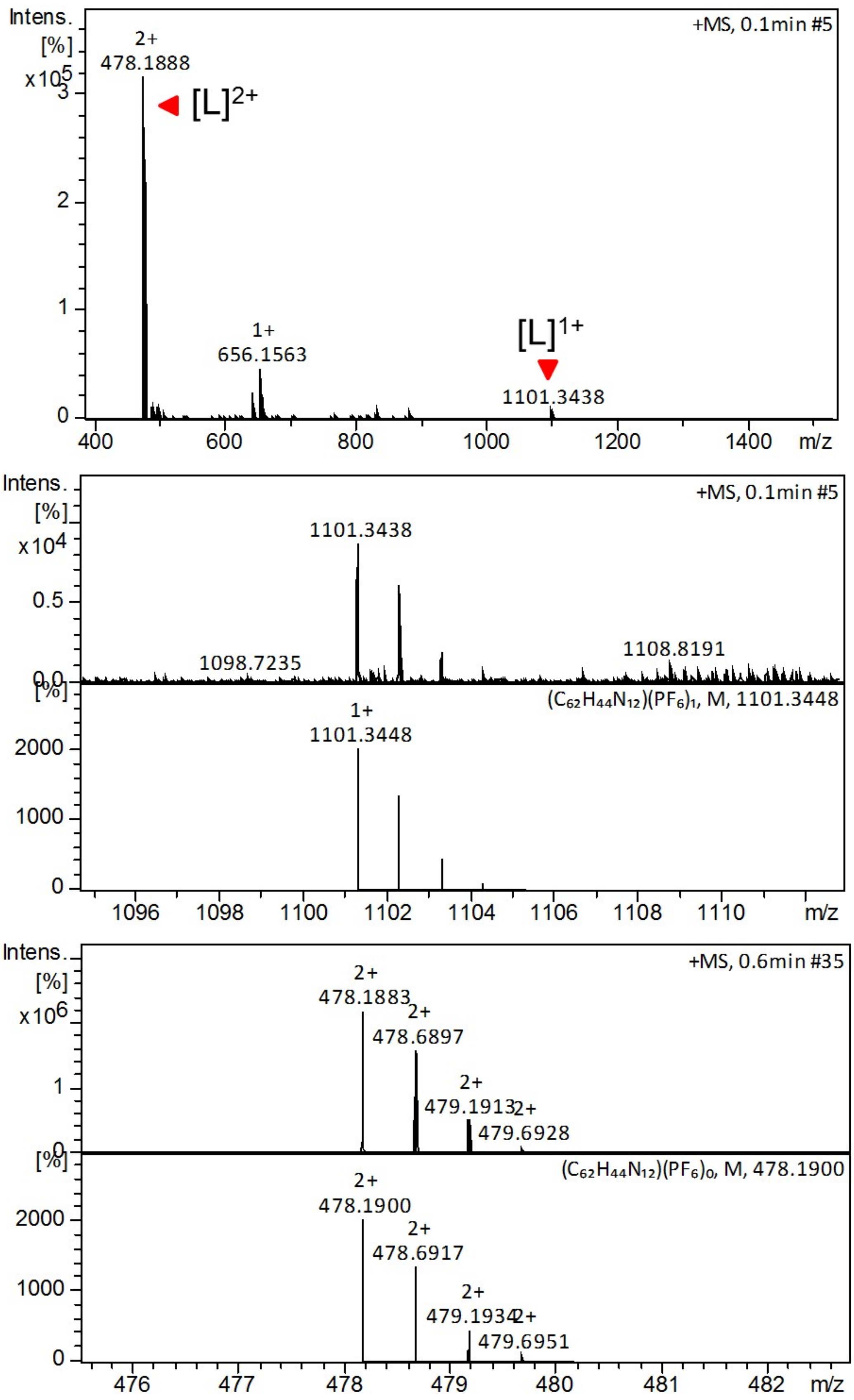

Figure S9. ESI-TOF-MS of ligand **L**·$(PF_6)_2$. The simulated and observed isotopic distributions of the +2 and +1 peaks are well matched.

3.2 Synthesis of Pd_6L_3 cage 1

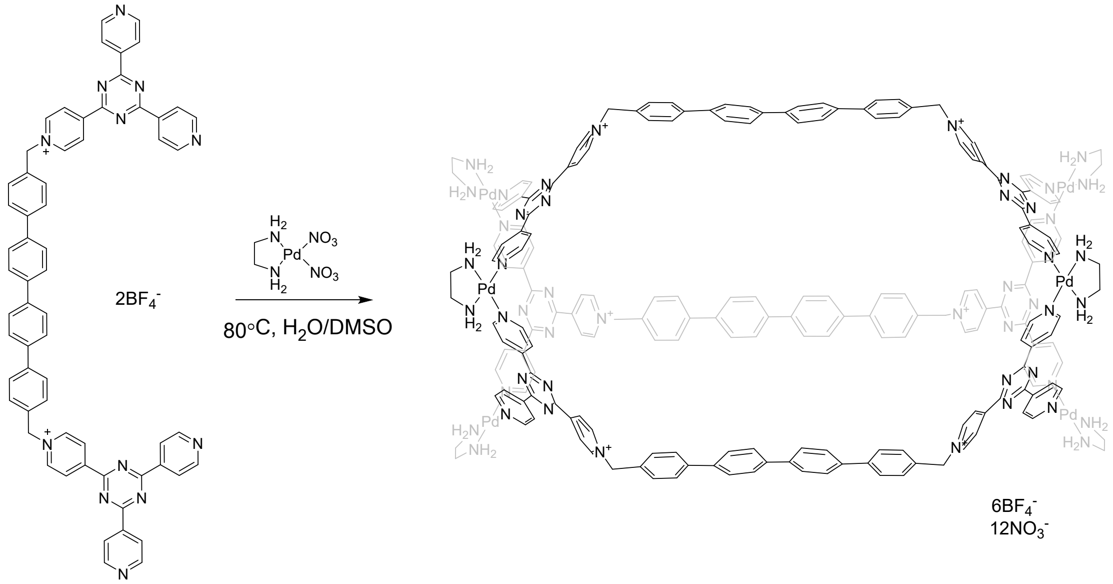

Scheme S2. Synthesis route of cage **1** in H_2O/DMSO (v/v = 4/1).

Synthesis route of cage 1: L·$(BF_4)_2$ (2.4 mg, 2 μmol) and enPd$(NO_3)_2$ (1.16 mg, 4 μmol) were dissolved in 0.8 mL of solvent (D_2O/DMSO-*d*$_6$, v/v = 4/1), and the reaction mixture was stirred vigorously at 80 °C for 30 min to afford a homogeneous solution. The quantitative formation of cage **1** was confirmed by ^{1}H NMR and ESI-TOF MS analyses. ^{1}H NMR (400 MHz, D_2O/DMSO-*d*$_6$, v/v = 4/1, 298K) δ 9.26 (d, *J* = 6.8 Hz, 2H), 9.21 (d, *J* = 6.0 Hz, 4H), 9.19 (d, *J* = 6.8 Hz, 2H), 8.76 (d, *J* = 6.0 Hz, 4H), 7.66 (d, *J* = 8.0 Hz, 2H), 7.59 (d, *J* = 8.4 Hz, 2H), 7.50(d, *J* = 8.0 Hz, 2H), 7.48 (d, *J* = 8.4 Hz, 2H), 5.95 (s, 2H). ESI-TOF-MS: m/z calcd for $[Pd_6L_3(BF_4)_{15}]^{3+}$ 1724.0124 found 1724.0135; m/z calcd for $[Pd_6L_3(BF_4)_{14}]^{4+}$ 1271.2542 found 1271.2591; m/z calcd for $[Pd_6L_3(BF_4)_{13}]^{5+}$ 999.6038 found 999.6065; m/z calcd for $[Pd_6L_3(BF_4)_{12}]^{6+}$ 818.6700 found 818.6714. The similar Pd_6L_3 assembly was also formed in D_2O/CD_3CN (v/v = 2/1) using L·$(PF_6)_2$ instead. ^{1}H NMR (400 MHz, D_2O/CD_3CN, v/v = 2/1, 298K) δ 9.49 (d, *J* = 6.0 Hz, 4H), 9.45 (d, *J* = 6.4 Hz, 2H), 9.43 (d, *J* = 6.4 Hz, 2H), 9.02 (d, *J* = 6.0, 4H), 7.86 (d, *J* = 8.4 Hz, 2H), 7.78 (m, 6H)， 6.18 (s, 2H). ESI-TOF-MS: m/z calcd for $[Pd_6L_3(PF_6)_{13}]^{5+}$ 1150.9071 found 1150.9079; m/z calcd for $[Pd_6L_3(PF_6)_{12}]^{6+}$ 934.9262 found 934.9285; m/z calcd for $[Pd_6L_3(PF_6)_{11}]^{7+}$ 780.6536 found 780.6582; m/z calcd for $[Pd_6L_3(PF_6)_{10}]^{8+}$ 664.9546 found 664.9555.

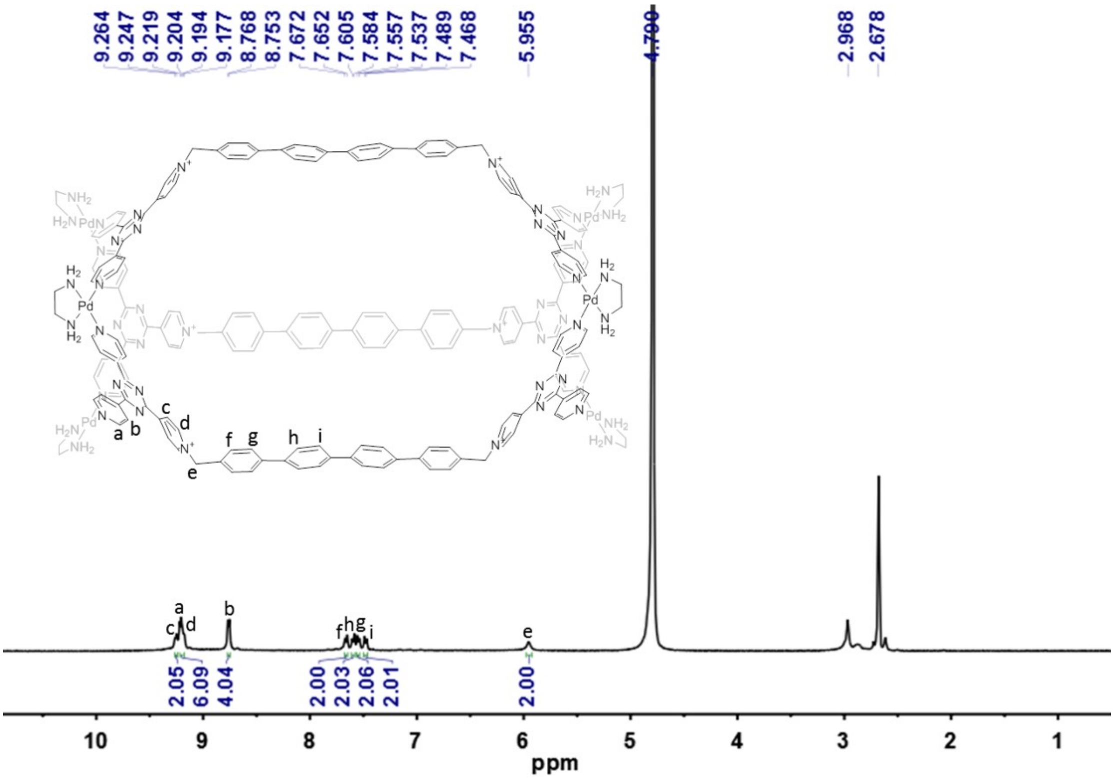

Figure S10. ^{1}H NMR spectrum (400 MHz, D_2O/DMSO-d_6, v/v = 4/1, 298 K) of cage **1**.

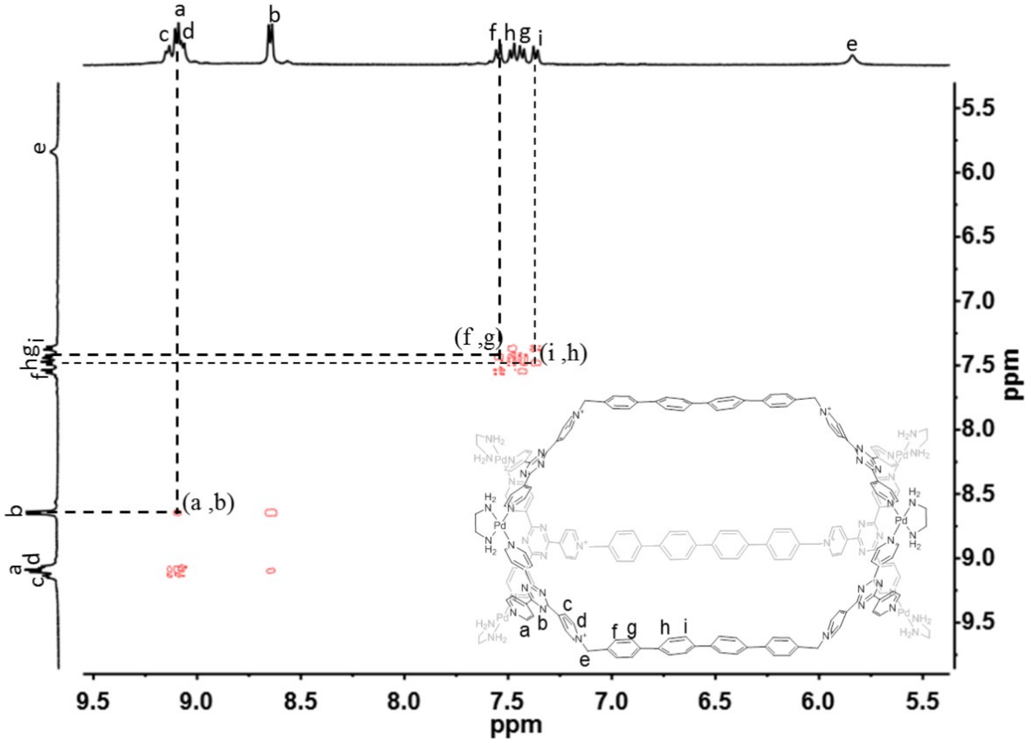

Figure S11. ^{1}H-^{1}H COSY NMR spectrum (400 MHz, D_2O/DMSO-d_6, v/v = 4/1, 298 K) of cage **1**.

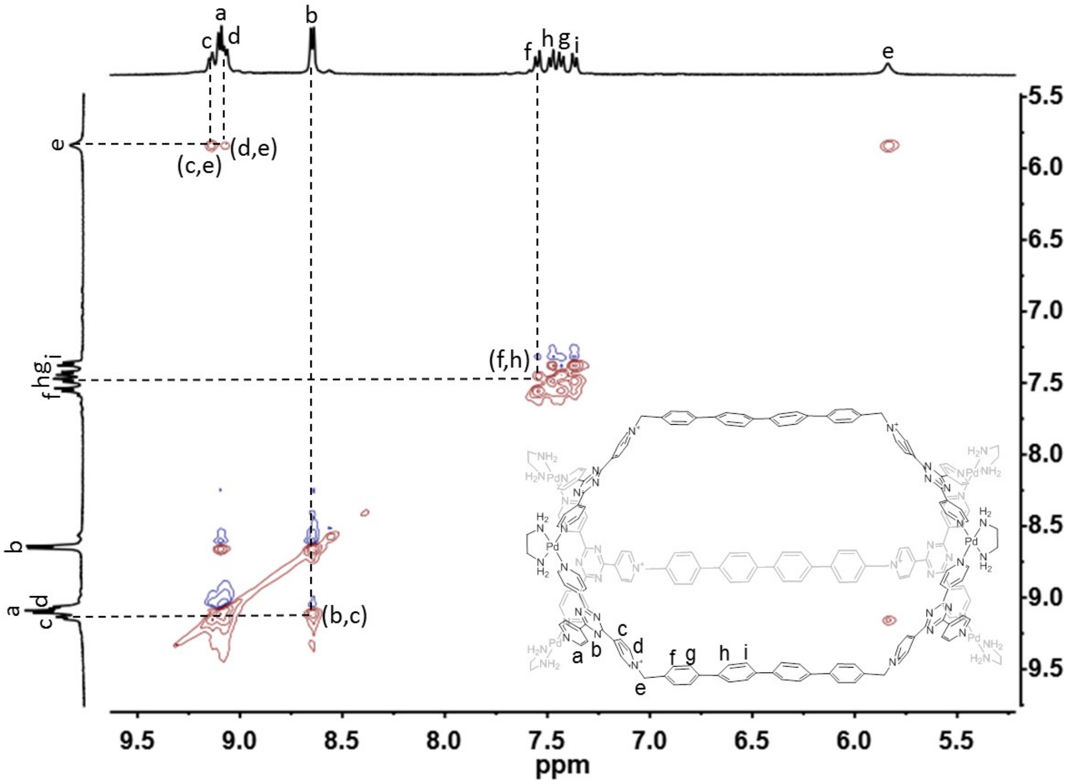

Figure S12. ^{1}H-^{1}H NOESY NMR spectrum (400 MHz, D_2O/DMSO-d_6, v/v = 4/1, 298 K) of cage **1**.

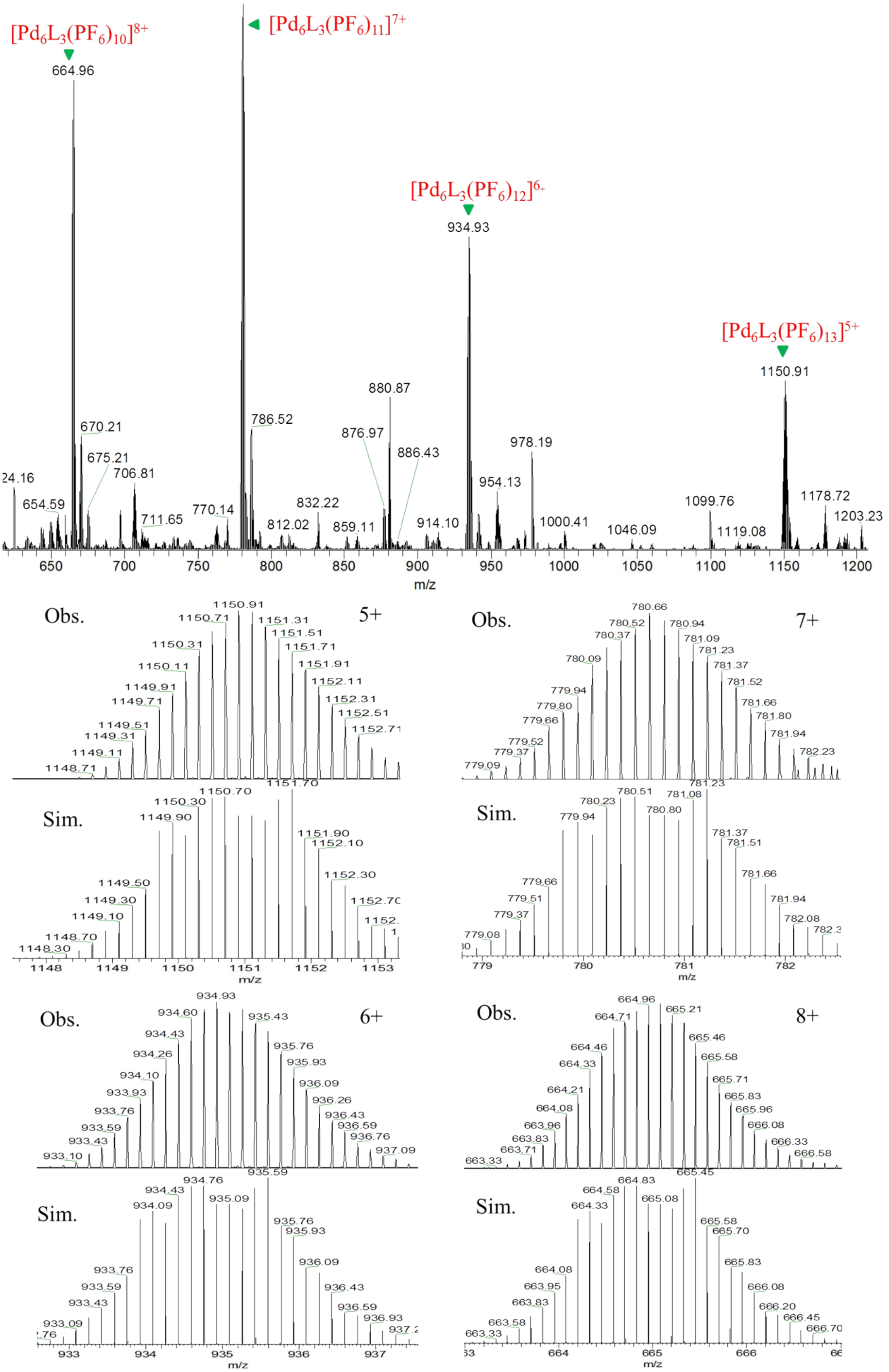

Figure S13. ESI-TOF-MS of cage **1** with inset showing the observed (Obs.) and simulated (Sim.) isotopic distribution of the 5+, 6+, 7+, 8+ peaks.

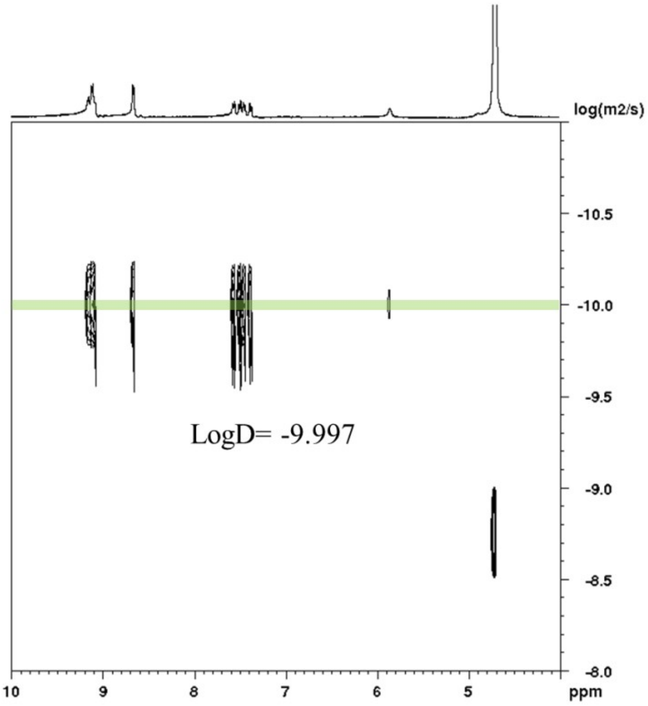

Figure S14. ^{1}H-^{1}H DOSY spectrum (400 MHz, D_2O/ DMSO-*d_6*, v/v = 4/1, 298 K) of cage **1**.

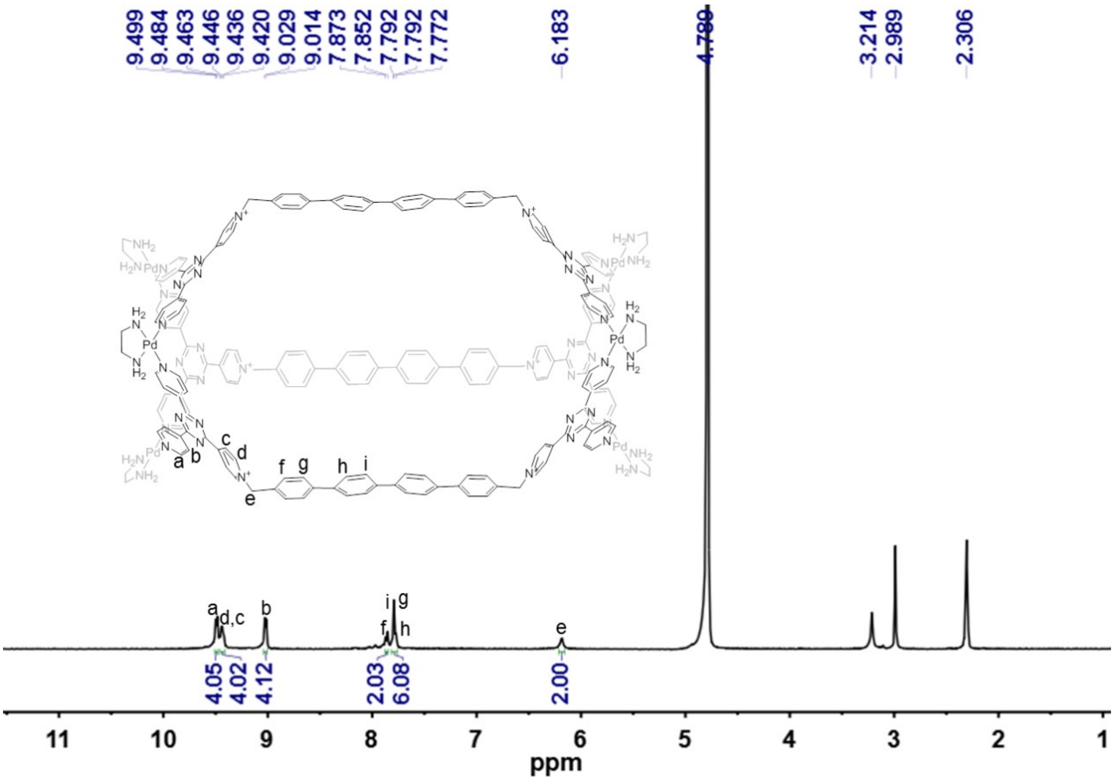

Figure S15. ^{1}H NMR spectrum (400 MHz, D_2O/CD_3CN, v/v = 2/1, 298 K) of cage **1**.

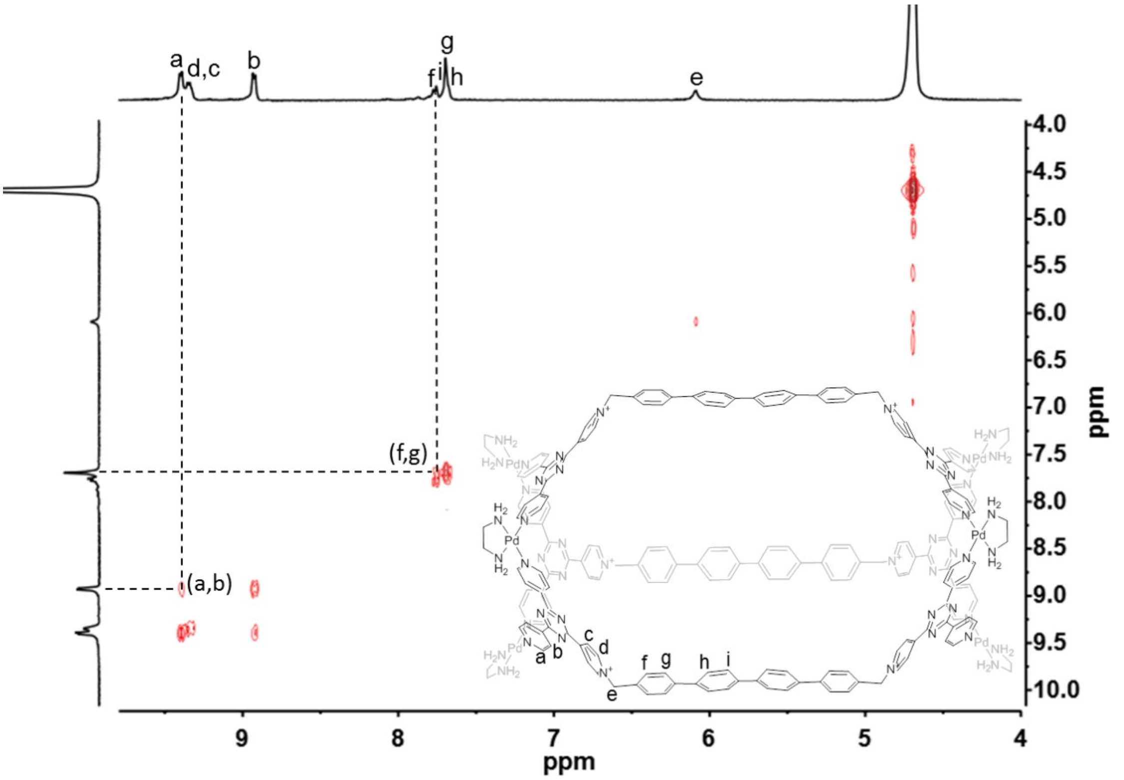

Figure S16. ^1H-^1H COSY NMR spectrum (400 MHz, D_2O/CD_3CN, v/v = 2/1, 298 K) of cage **1**.

4. Photophysical properties of cage 1

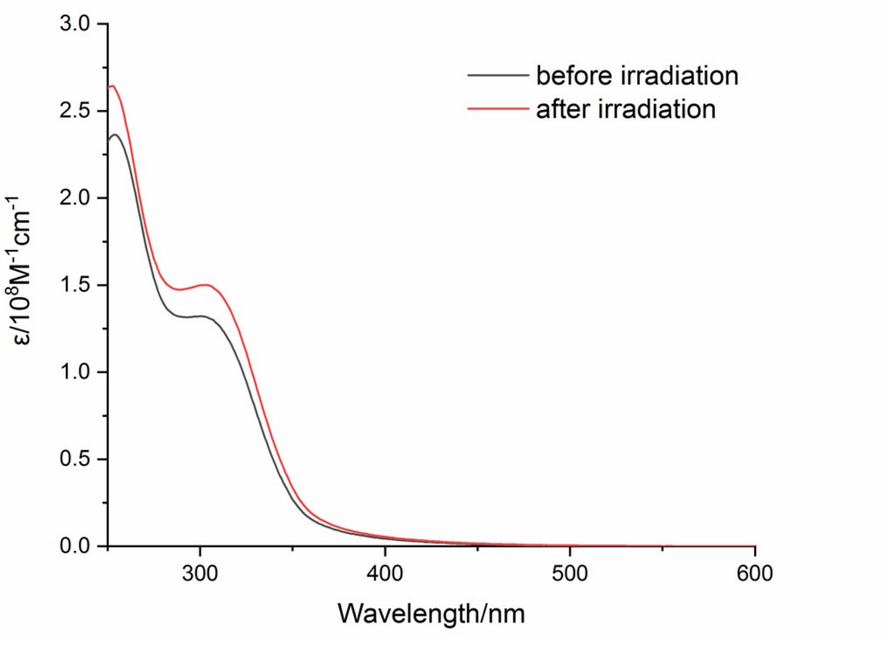

Figure S17. UV-Vis diffuse reflectance spectra of cage **1** in H_2O/DMSO (v/v = 4/1) solution before (black line) and after (red line) irradiation.

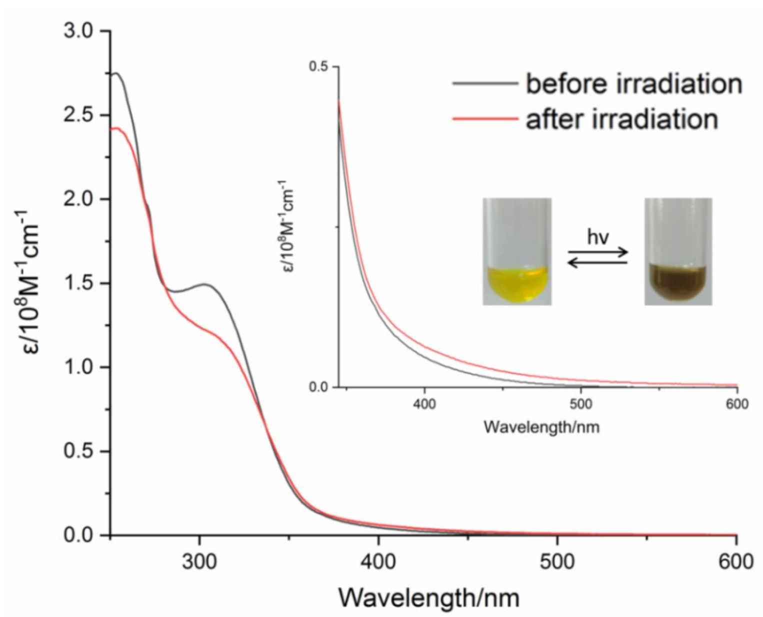

Figure S18. The UV-vis absorption spectra of 100 equivalents of isochroman added to cage **1** in a H_2O/DMSO (v/v = 4/1) solution are shown before (black line) and after (red line) irradiation (xenon lamp; 200 mW/cm^2). The insets show the color changes of isochroman$\subset$cage in the local UV-vis range (340–600 nm) before and after illumination, and the system returns to its original color after being exposed to air for 48 h.

Cyclic Voltammetry. To facilitate the assignment of the redox peaks in CVs of the ligand and cage **1,** we conducted some simple control experiments under the same conditions for comparison, including CV measurements of **2,4,6-trimethyl-1,3,5-triazine** (Figure S19), **p-quaterphenyl** (Figure S20), 2,4,6-tris(4-pyridyl)-1,3,5-triazine (**4-TPT**) (Figure S21), (N,N′,N″-trimethyl-2,4,6-tris(4-pyridyl)-1,3,5-triazine Tris(hexafluorophosphate) (**Me_3TPT**·$(PF_6)_3$) (Figure S22) and 1-benzyl-4-(4,6-di(pyridin-4-yl)-1,3,5-triazin-2-yl)pyridin-1-ium hexafluorophosphate (**Bz-TPT**·(PF_6)) (Figure S23). **2,4,6-Trimethyl-1,3,5-triazine** and **p-quaterphenyl** exhibited no discernible redox peaks within the applied potential window (0 − −2.0 V vs. Ag/AgCl). **4-TPT** exhibited a pair of reversible redox peaks ($E_{1/2}$ = −0.92 V vs. Ag/AgCl). **$Me_3TPT(PF_6)_3$** displayed three well-defined reduction peaks at $E_{1/2}$ = −0.32, −0.63, and −1.04 V (vs. Ag/AgCl), corresponding to the reduction of pyridinium groups from the cationic state to the neutral state. The final reduction peak at $E_{1/2}$ = −1.57 V corresponds to one single-electron redox process of triazine unit. For **Bz-TPT**·(PF_6), the reversible redox couple (ΔE_p = 84 mV, $E_{1/2}$ = −0.40 V vs. Ag/AgCl, $I_{pc}/I_{pa} \sim 1.0$), corresponds to the single-electron redox process of pyridinium group.

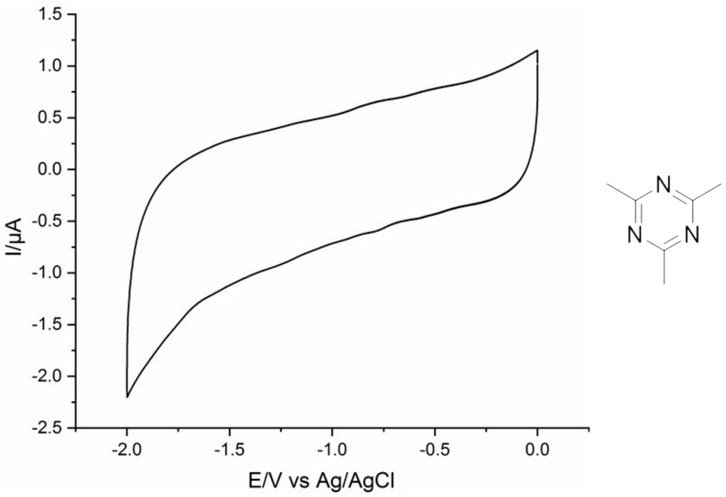

Figure S19. CV of 2,4,6-trimethyl-1,3,5-triazine (1.0 mM) in Bu_4NPF_6 (0.1 M) DMSO solution at a scan rate of 0.1 V/s.

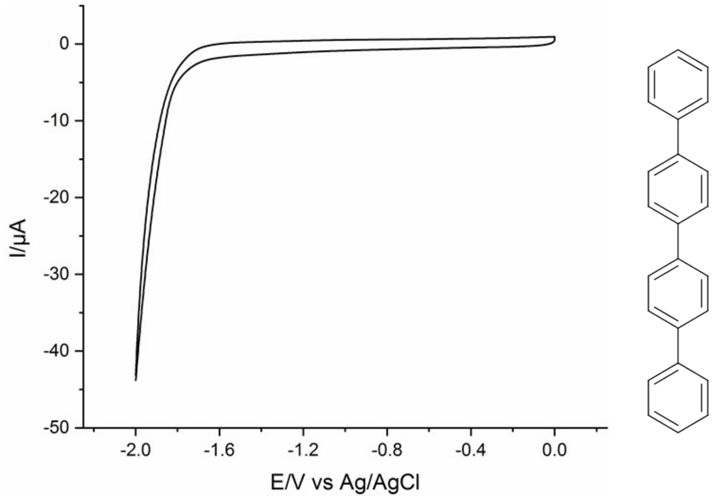

Figure S20. CV of p-quaterphenyl (0.5 mM) in Bu_4NPF_6 (0.1 M) DMSO solution at a scan rate of 0.1 V/s.

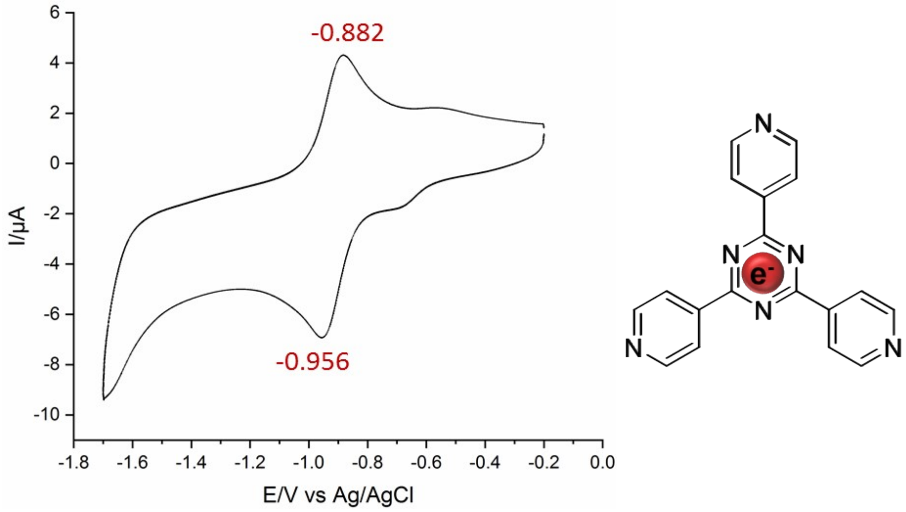

Figure S21. CV of 4-TPT (1.0 mM) in DMSO solution containing 0.1 M Bu_4NPF_6, recorded at a scan rate of 0.1 V/s. The reversible redox couple corresponds to one-electron redox processes of the triazine moiety ($E_{1/2}$ = -0.92 V vs. Ag/AgCl).

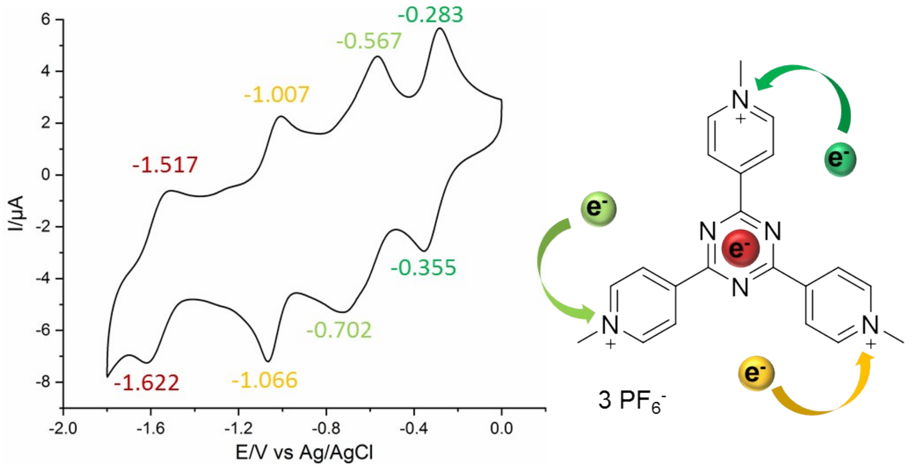

Figure S22. CV of $Me_3tpt(PF_6)_3$ (1.0 mM) in DMSO solution containing 0.1 M Bu_4NPF_6, recorded at a scan rate of 0.1 V/s. The first three redox couples correspond to three single-electron redox processes of pyridinium groups ($E_{1/2}$ = -0.32 V, -0.63V and -1.04 V vs. Ag/AgCl), involving the reduction from the cationic state to the neutral state. The final redox couple corresponds to one single-electron redox process of triazine unit ($E_{1/2}$ = -1.62 V vs. Ag/AgCl).

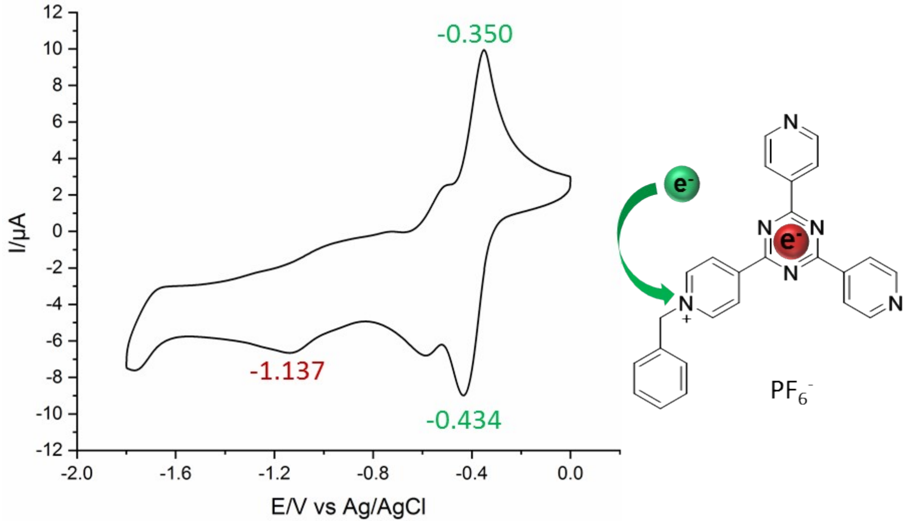

Figure S23. CV of Bz-TPT (1.0 mM*)* in DMSO solution containg 0.1 M Bu_4NPF_6, recorded at a scan rate of 0.1 V/s. The reversible redox couple (ΔE_p = 84 mV, $E_{1/2}$ = -0.39 V vs. Ag/AgCl, $I_{pc}/I_{pa} \sim 1.0$) corresponds to the single-electron redox process of pyridinium group. The irreversible reduction potential at -1.14 V arises from one-electron reduction processes of the triazine moiety.

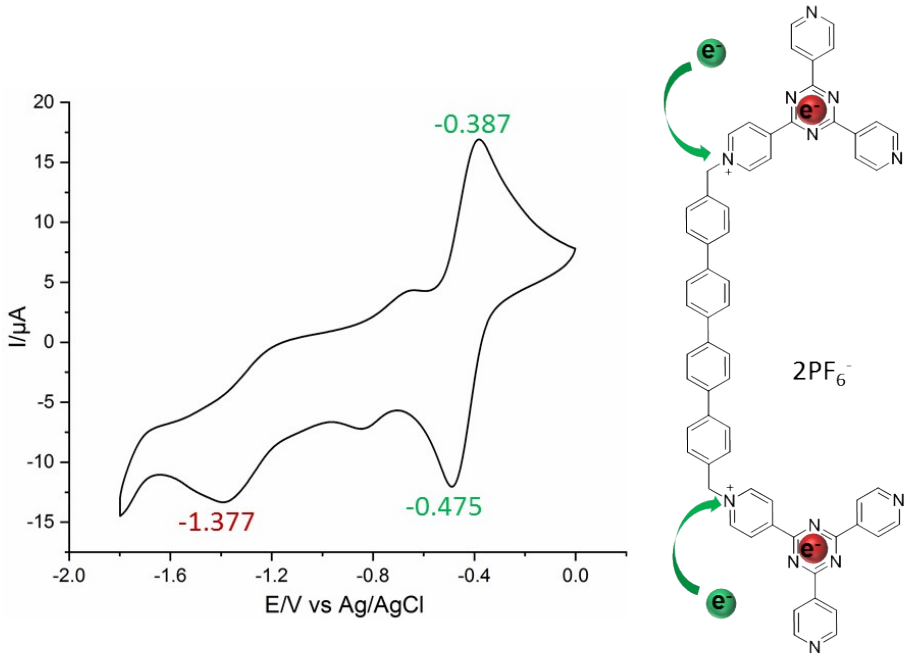

Figure S24. CV of **L**$\cdot(PF_6)_2$ (0.5 mM) in DMSO solution contaning 0.1 M Bu_4NPF_6, recorded at a scan rate of 0.1 V/s. One reversible pyridinium group reduction occurs at $E_{1/2}$ = -0.43 V vs. Ag/AgCl (ΔE_p = 88 mV, I_{pc}/I_{pa} ~ 1.0), while the triazine units exhibit an irreversible reduction potential at -1.38 V vs. Ag/AgCl.

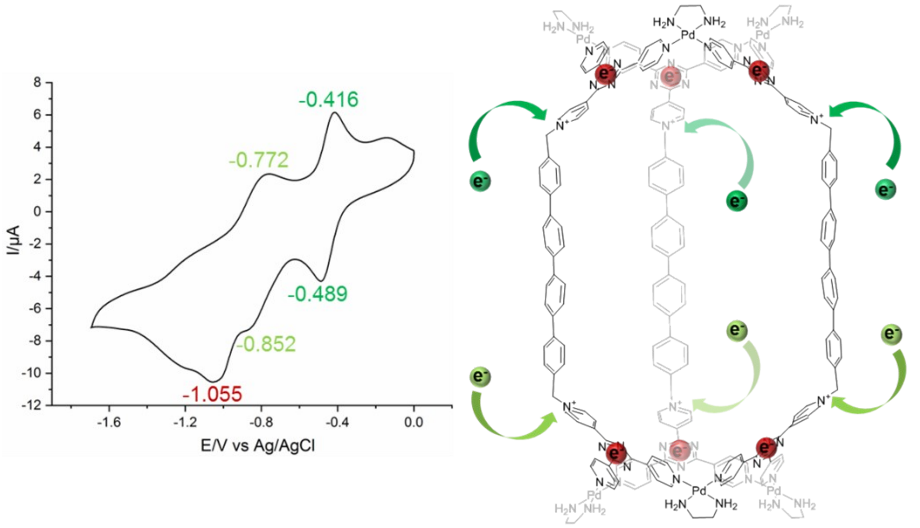

Figure S25. CV of **cage 1** (0.17 mM) in Bu_4NPF_6 (0.1 M) DMSO solution at a scan rate of 0.1 V/s. Cage 1 exhibited two well-defined reversible reduction waves at -0.45 V and -0.81 V (vs. Ag/AgCl), assigned to sequential single-electron reductions at the pyridinium nitrogen centers. The final reduction event, observed at -1.055 V (vs. Ag/AgCl), likely arises from an electron transfer process localized at the triazine ring.

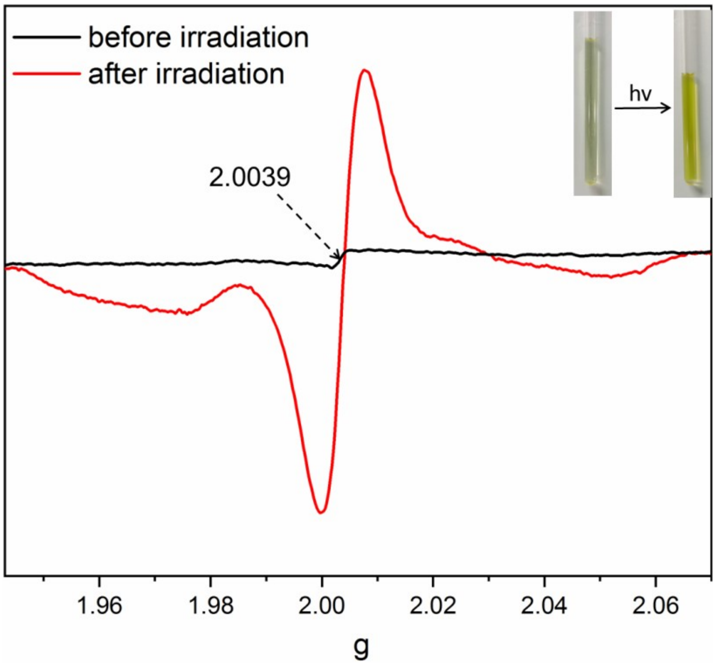

Figure S26. ESR spectra of cage **1** in H_2O/CH_3CN (v/v = 2/1) solution before (black line) and after (red line) irradiation at 100 K under N_2. The g-factor is 2.0039.

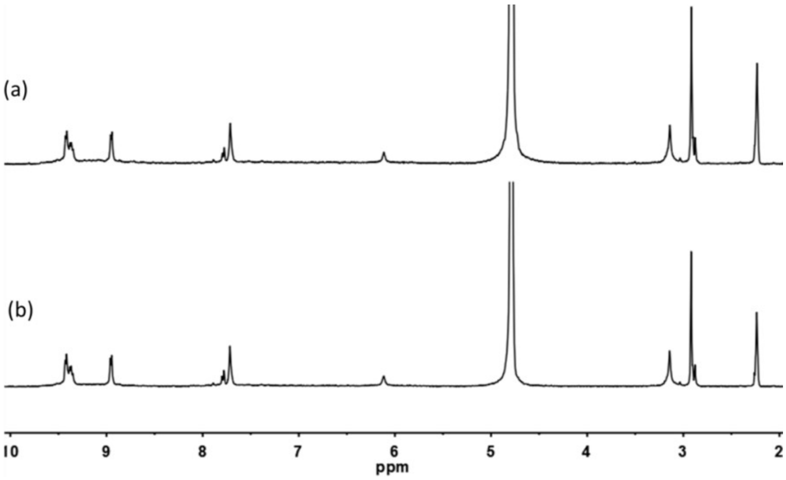

Figure S27. ^1H NMR spectra (400 Hz, D_2O/CD_3CN, v/v = 2/1, 298 K) cage 1 (a) before and (b) after 2 h UV irradiation (365 nm) under N_2.

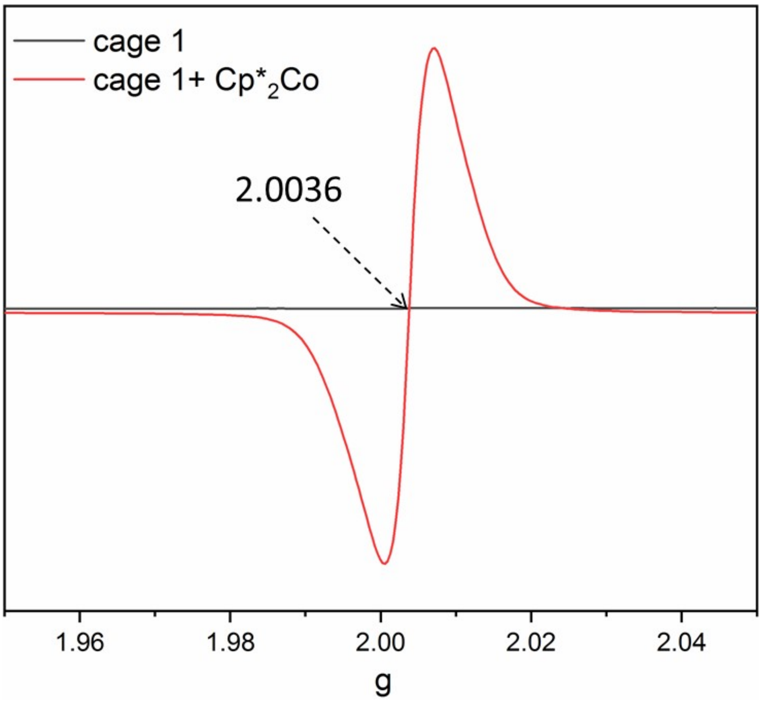

Figure S28. The ESR spectra of cage **1** (in H_2O/DMSO, v/v = 4/1) recorded before (black line) and after (red line) the addition of Cp*$_2$Co (ca. 6 equiv). The g-factor is 2.0036.

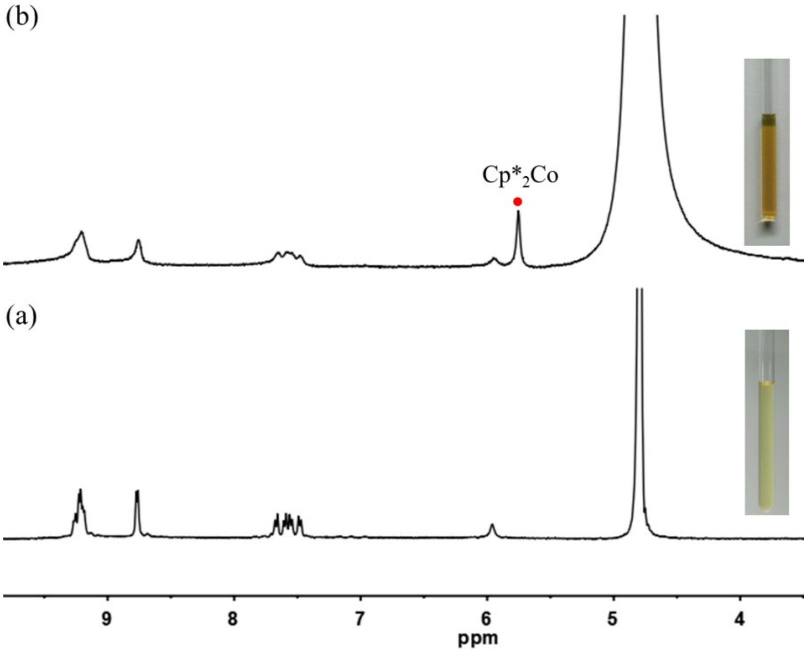

Figure S29. ^{1}H NMR spectra (400 MHz, D_2O/DMSO-d_6, v/v = 4/1, 298 K) of cage **1** before (a) and after (b) addition of Cp*$_2$Co.

5. Procedure for photocatalysis experiment

The photooxidation reaction was performed with isochroman, 7-bromoisochroman, phthalan, 2,3-dihydrobenzofuran, and xanthene. Generally, substrate (100 equiv.) was added into the D_2O/DMSO-d_6 (v/v = 4/1) solution (0.8 mL) containing $(enPd)_6L_3$ catalyst (0.0007 mmol, 1 equiv.). The mixture was irradiated under purple LEDs (365 nm) with magnetic stirring and oxygen as an oxidant at room temperature unless otherwise noted. After the reaction, the product was extracted with $CDCl_3$ (2× 0.5 mL), which was subjected to ^1H NMR without purification. The conversions of reaction are determined using 1,3,5-trimethoxybenzene as the internal standard (0.014 mmol). Control experiments were carried out in the absence of catalysis, light, or under N_2 atmosphere.

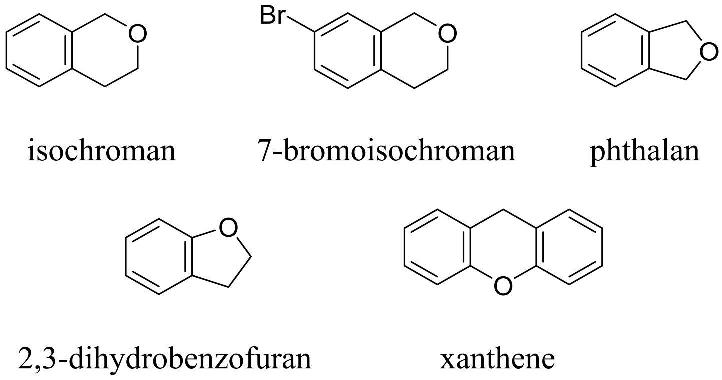

Scheme S3. Substrate scope for photooxidation

5.1 The photocatalysis performance of 1

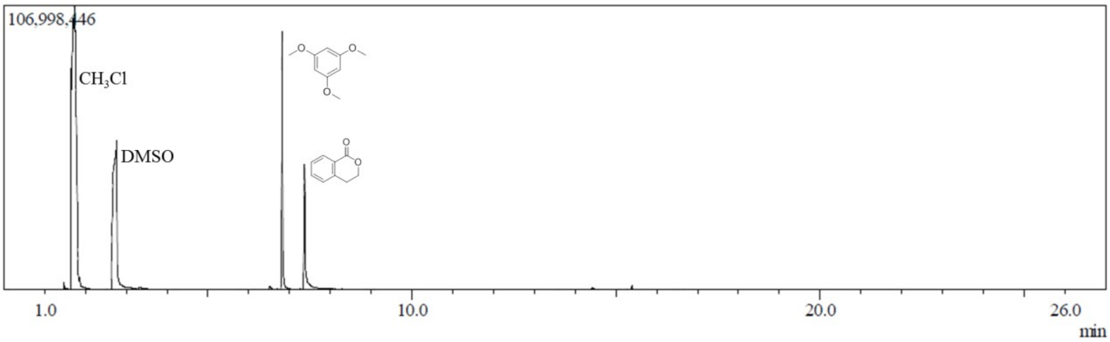

Figure S30. Gas chromatography of photooxidation product of isochroman with the catalysis of cage **1** (1 mol% catalyst loading).

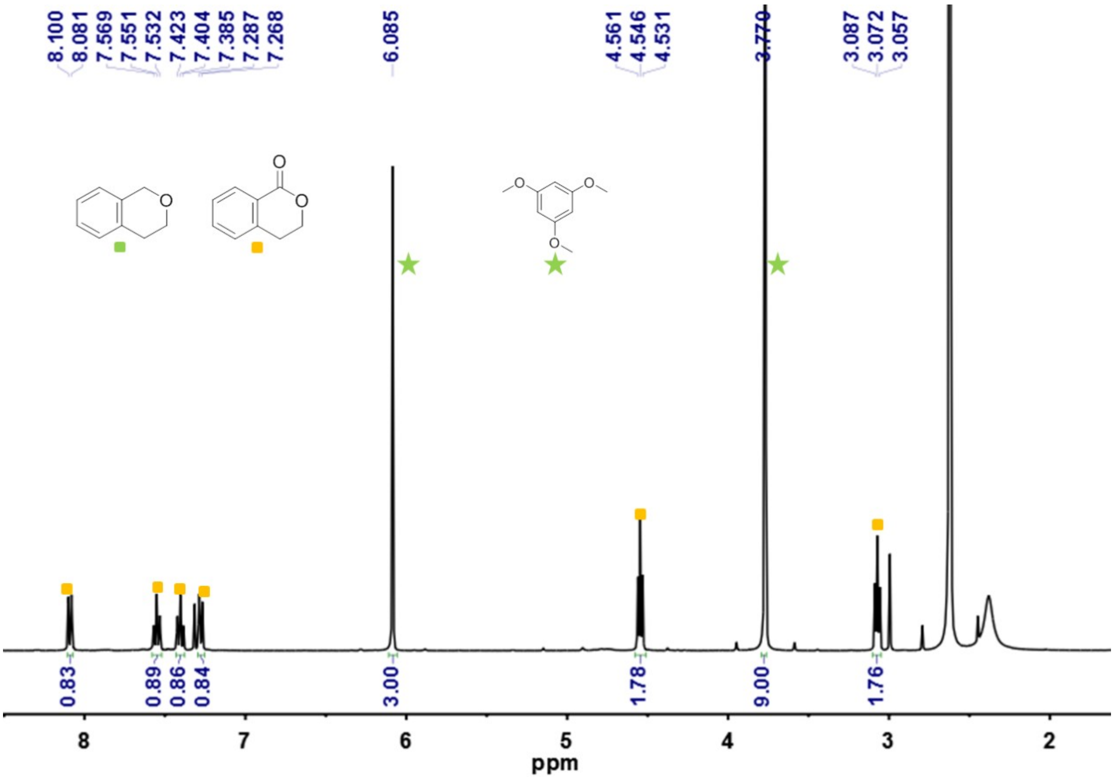

Figure S31. ^{1}H NMR spectrum (400 MHz, $CDCl_3$, 298 K) of photooxidation product of isochroman with the catalysis of cage **1** (1 mol% catalyst loading). 1,3,5-trimethoxybenzene was used as internal standard.

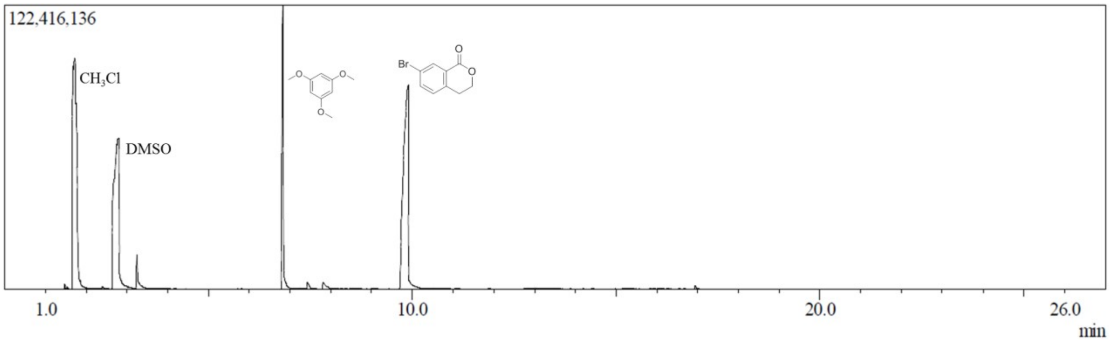

Figure S32. Gas chromatography of photooxidation product of 7-bromoisochroman with the catalysis of cage **1** (1 mol% catalyst loading).

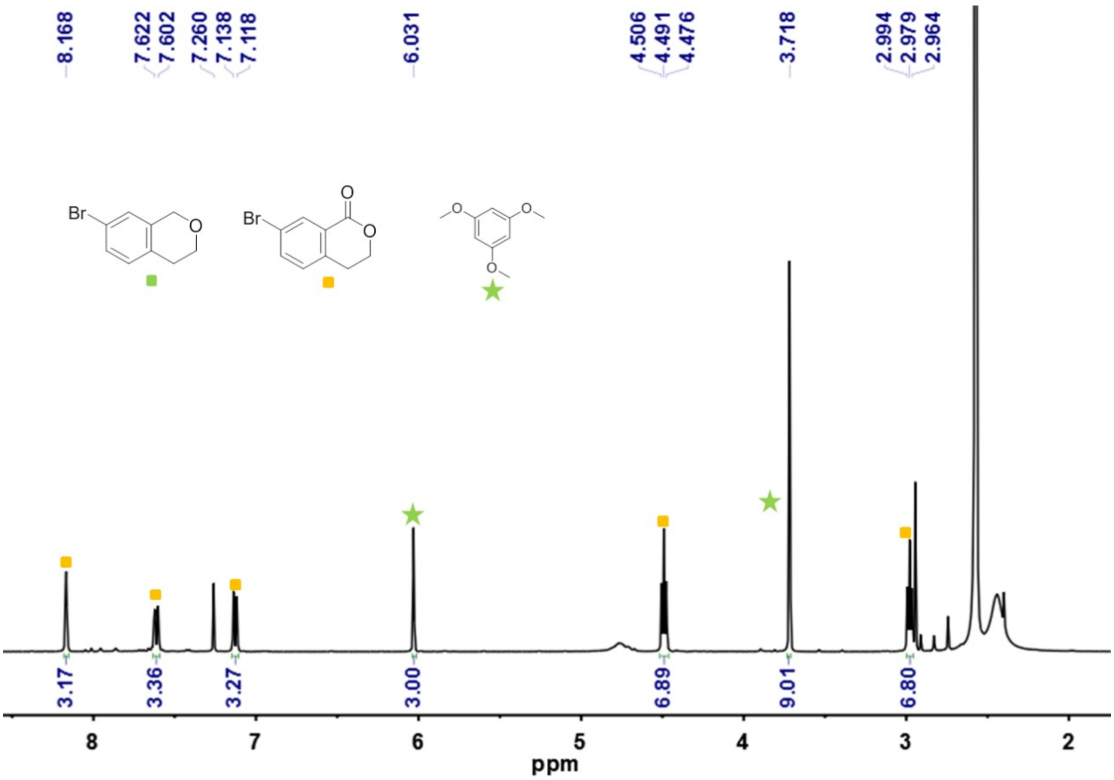

Figure S33. ¹H NMR spectrum (400 MHz, $CDCl_3$, 298 K) of photooxidation product of 7-bromoisochroman with the catalysis of cage **1** (1 mol% catalyst loading). 1,3,5-trimethoxybenzene was used as internal standard.

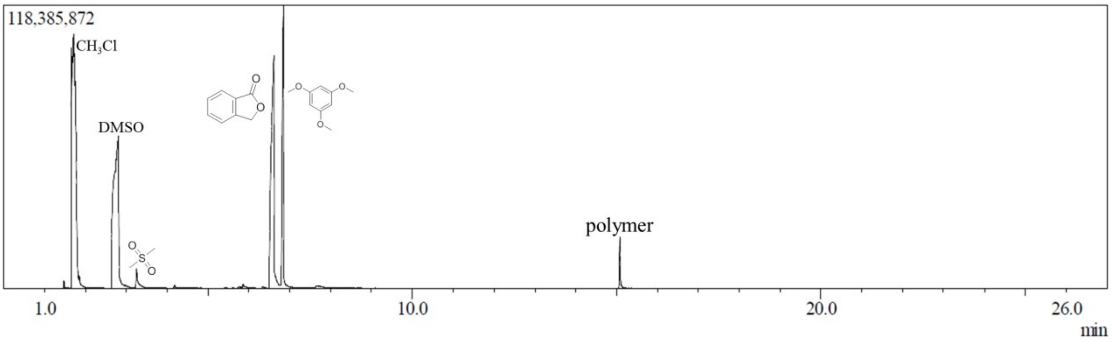

Figure S34. Gas chromatography of photooxidation product of phthalan with the catalysis of cage **1** (1 mol% catalyst loading).

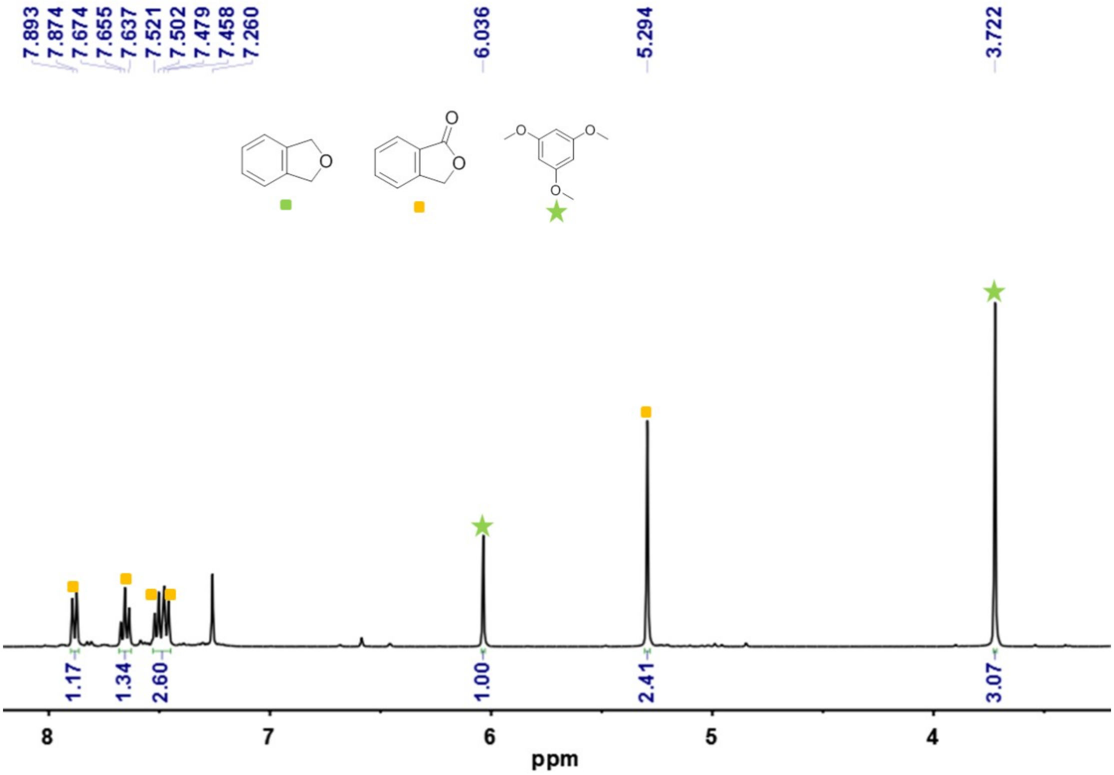

Figure S35. ^{1}H NMR spectrum (400 MHz, $CDCl_3$, 298 K) of photooxidation product of phthalan with the catalysis of cage **1** (1 mol% catalyst loading). 1,3,5-trimethoxybenzene was used as internal standard.

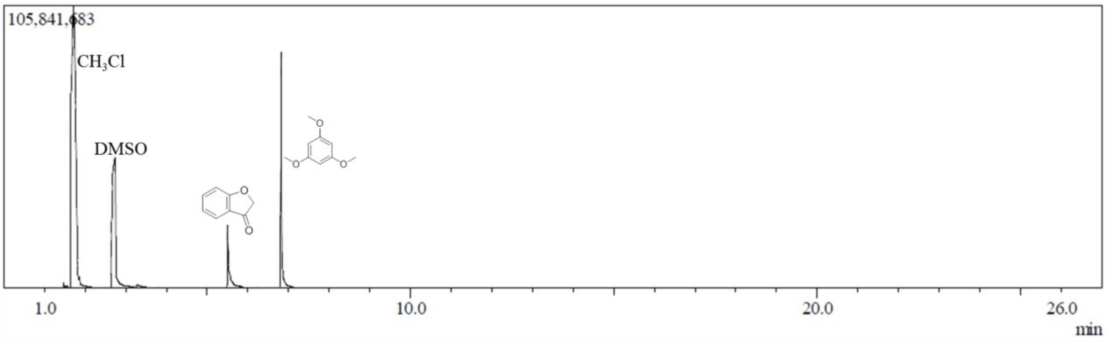

Figure S36. Gas chromatography of photooxidation product of 2,3-dihydrobenzofuran with the catalysis of cage **1** (1 mol% catalyst loading).

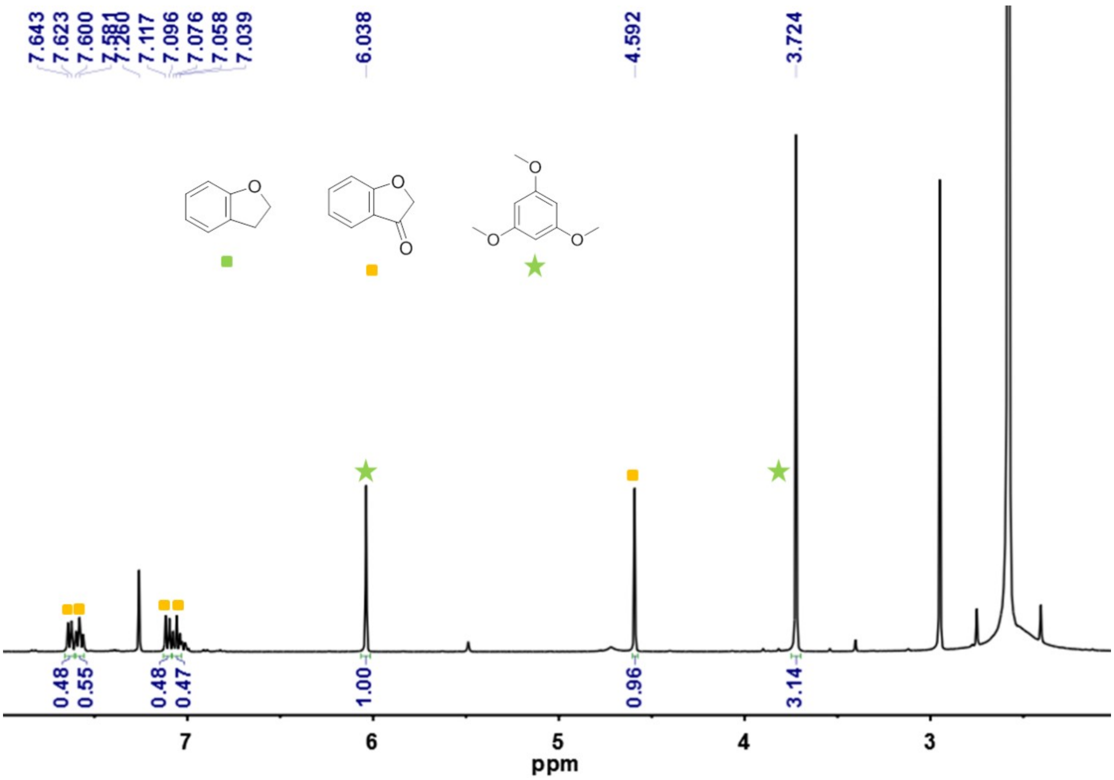

Figure S37. ^1H NMR spectrum (400 MHz, $CDCl_3$, 298 K) of photooxidation product of 2,3-dihydrobenzofuran with the catalysis of cage **1** (1 mol% catalyst loading). 1,3,5- trimethoxybenzene was used as internal standard.

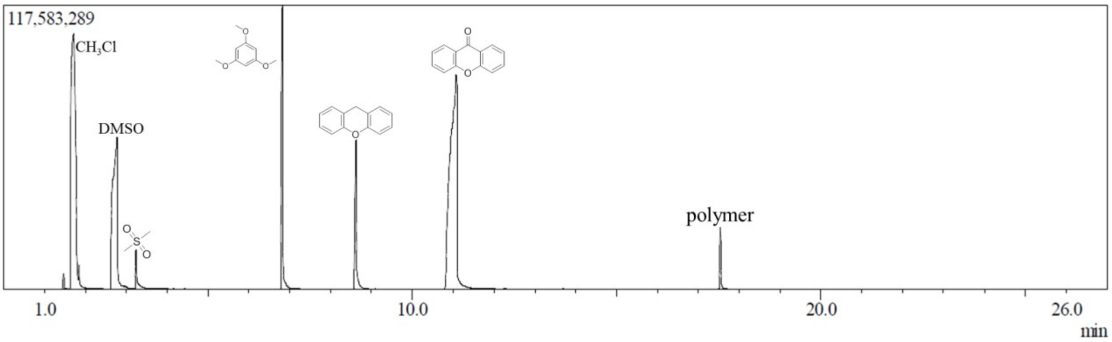

Figure S38. Gas chromatography of photooxidation product of xanthene with the catalysis of cage **1** (1 mol% catalyst loading).

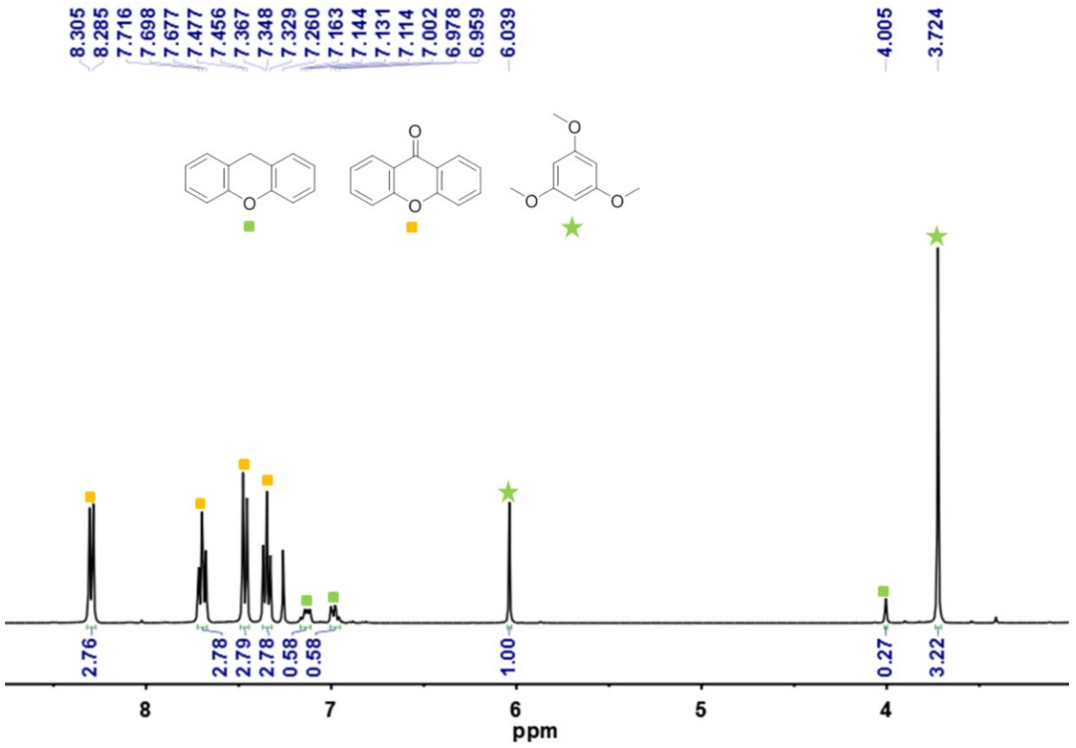

Figure S39. ^{1}H NMR spectrum (400 MHz, $CDCl_3$, 298 K) of photooxidation product of xanthene with the catalysis of cage **1** (1 mol% catalyst loading). 1,3,5-trimethoxybenzene was used as internal standard.

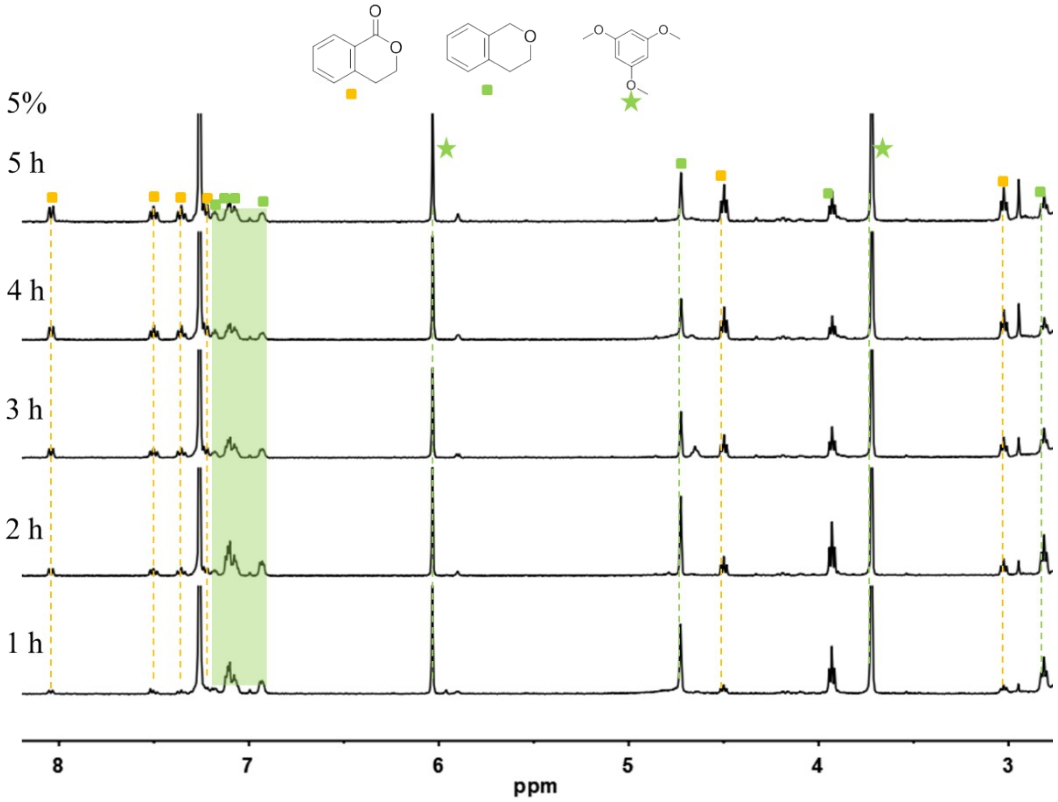

Figure S40. ^{1}H NMR (400MHz, $CDCl_3$, 298 K) of cage **1**-catalysed isochroman photo-oxidation reaction over 5 hours (with catalyst loading of 5% and a substrate concentration of 0.004 M, under 24 W 365 nm LEDs).

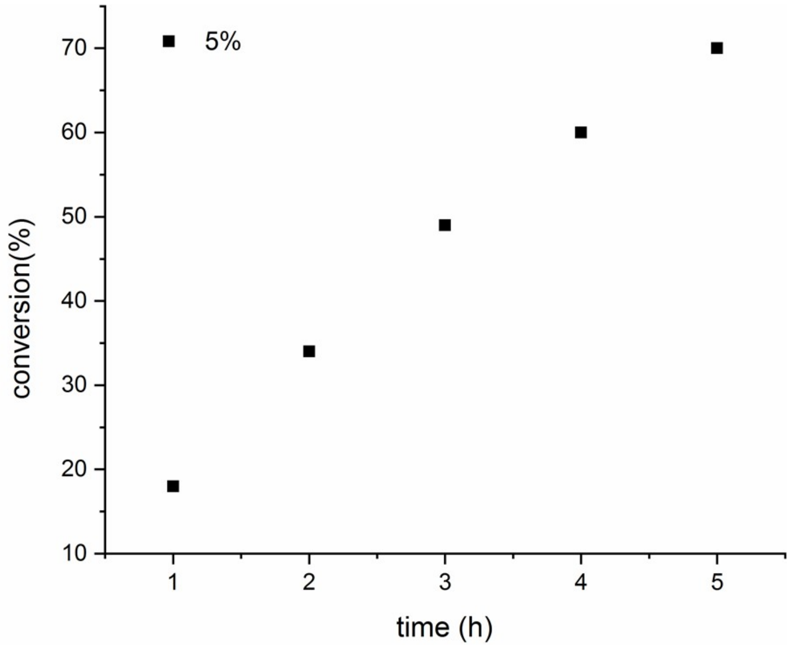

Figure S41. Conversion curves for cage **1**-catalysed isochroman photo-oxidation over 5 hours (with catalyst loading of 5% and a substrate concentration of 0.004 M, under 24 W 365 nm LEDs).

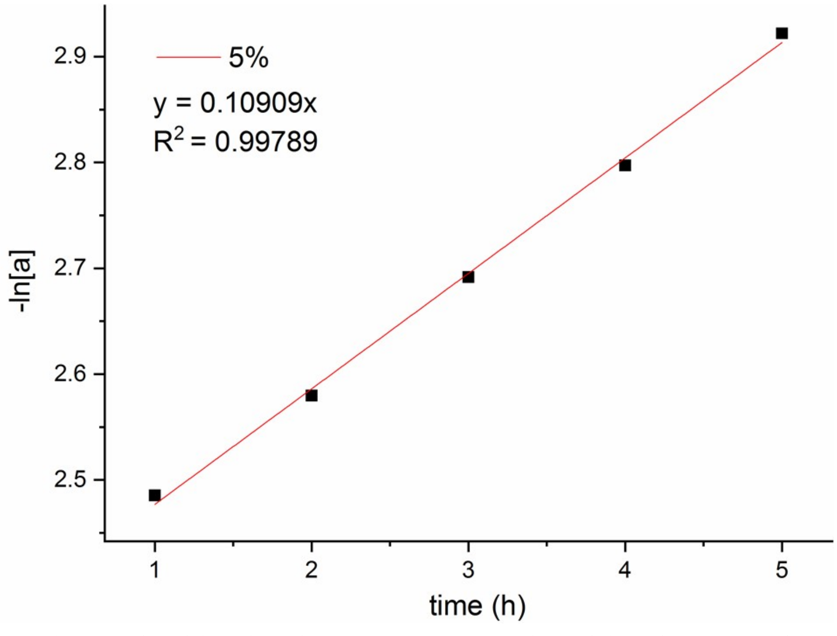

Figure S42. First-order kinetic plot of cage **1**-catalysed isochroman photo-oxidation reaction over 5 hours (with catalyst loading of 5% and a substrate concentration of 0.004 M, under 24 W 365 nm LEDs).

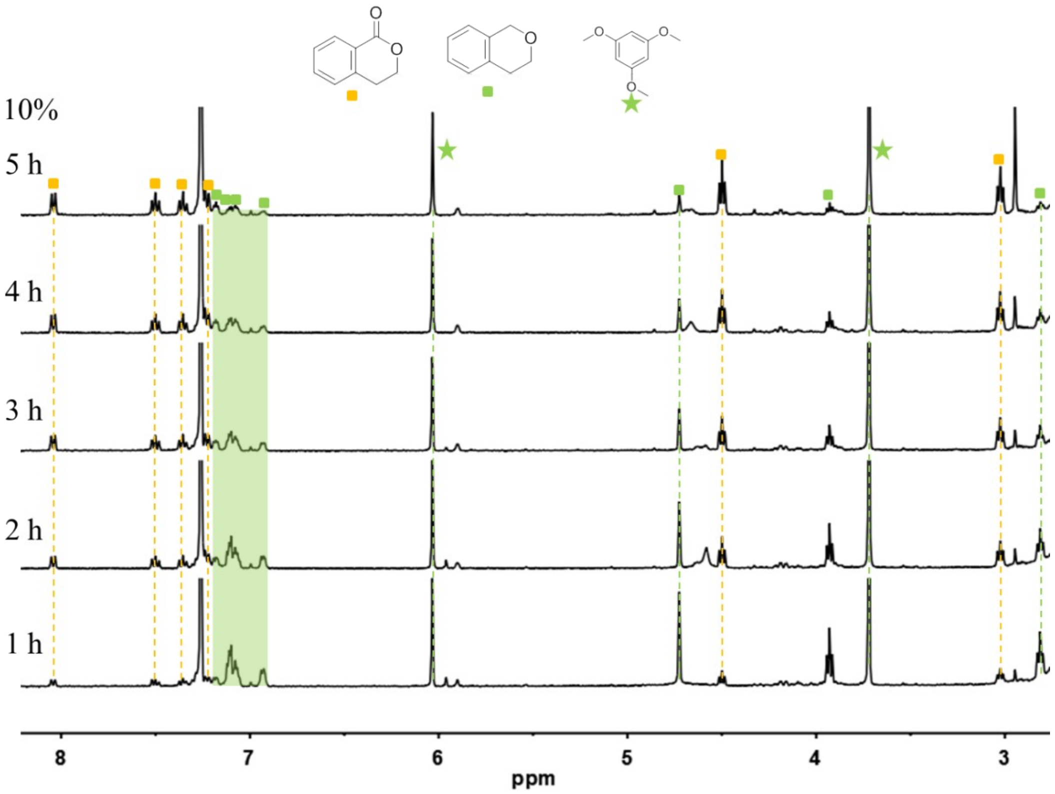

Figure S43. ^{1}H NMR (400MHz, $CDCl_3$, 298 K) of cage **1**-catalysed isochroman oxidation reaction over 5 hours (with catalyst loading of 10% and a substrate concentration of 0.004 M, under 24 W 365 nm LEDs).

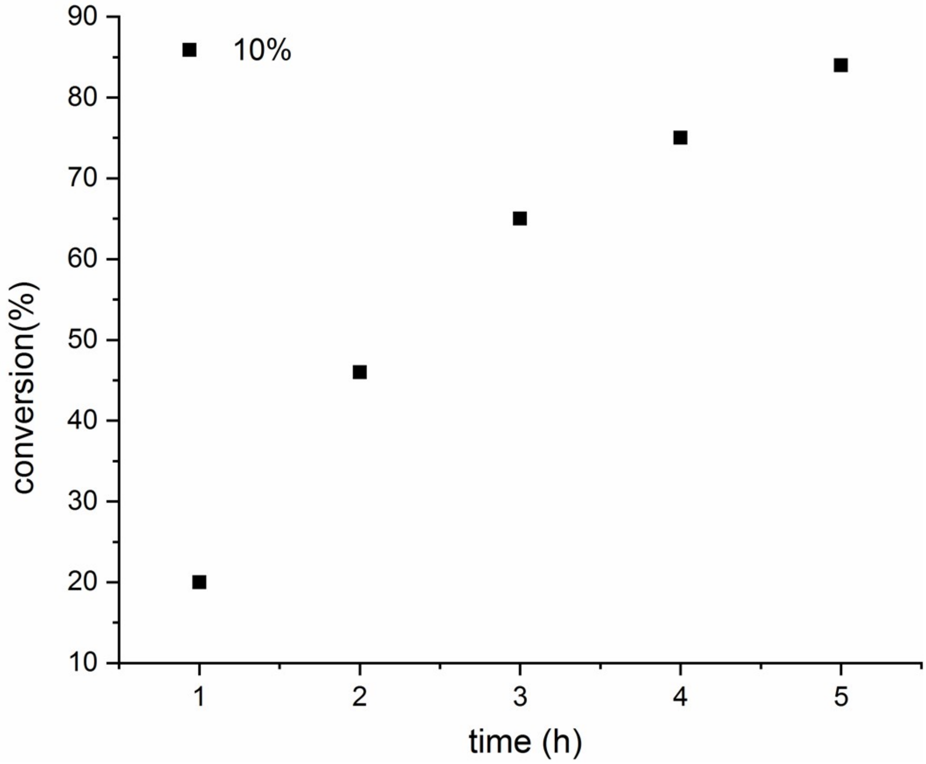

Figure S44. Conversion curves for cage **1**-catalysed isochroman photo-oxidation over 5 hours (with catalyst loading of 10% and a substrate concentration of 0.004 M, under 24 W 365 nm LEDs).

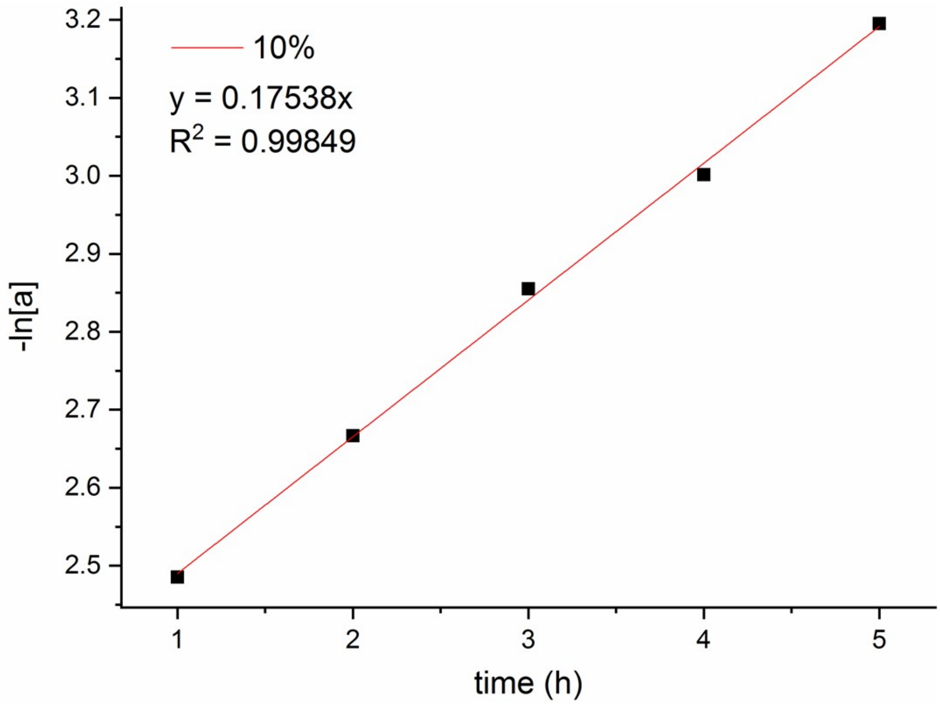

Figure S45. First-order kinetic plot of cage **1**-catalysed isochroman oxidation reaction over 5 hours (with catalyst loading of 10% and a substrate concentration of 0.004 M, under 24 W 365 nm LEDs).

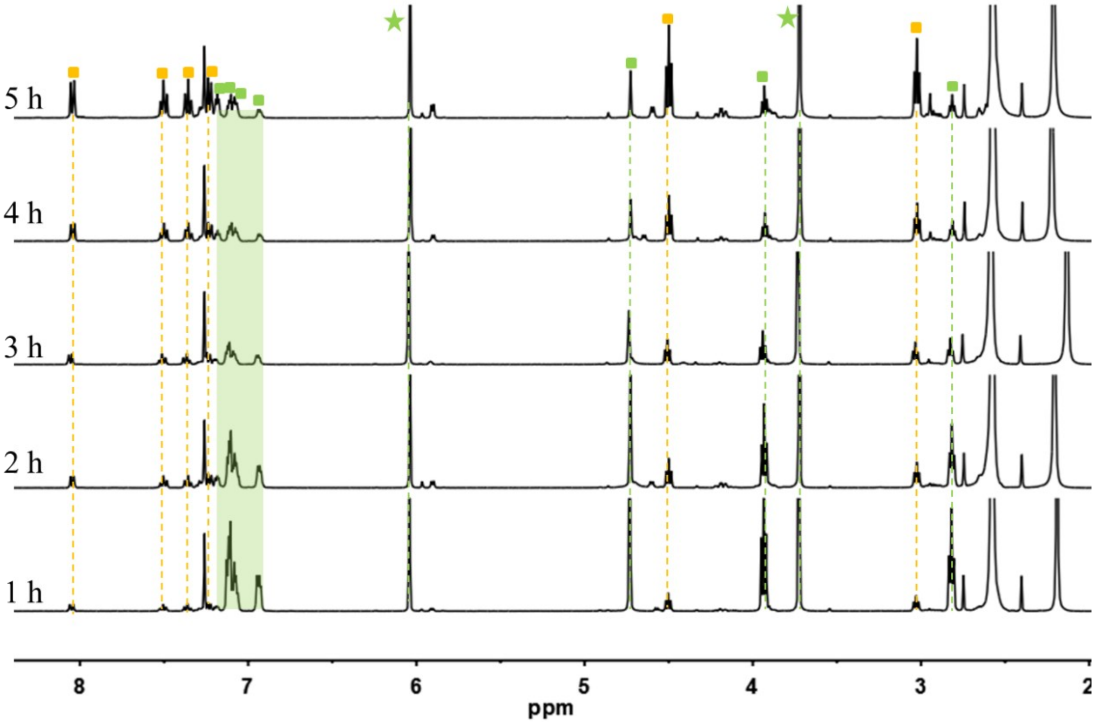

Figure S46. ^{1}H NMR (400MHz, $CDCl_3$, 298 K) of cage **1**-catalysed isochroman oxidation reaction over 5 hours (with catalyst loading of 10% and a substrate concentration of 0.008 M, under 24 W 365 nm LEDs).

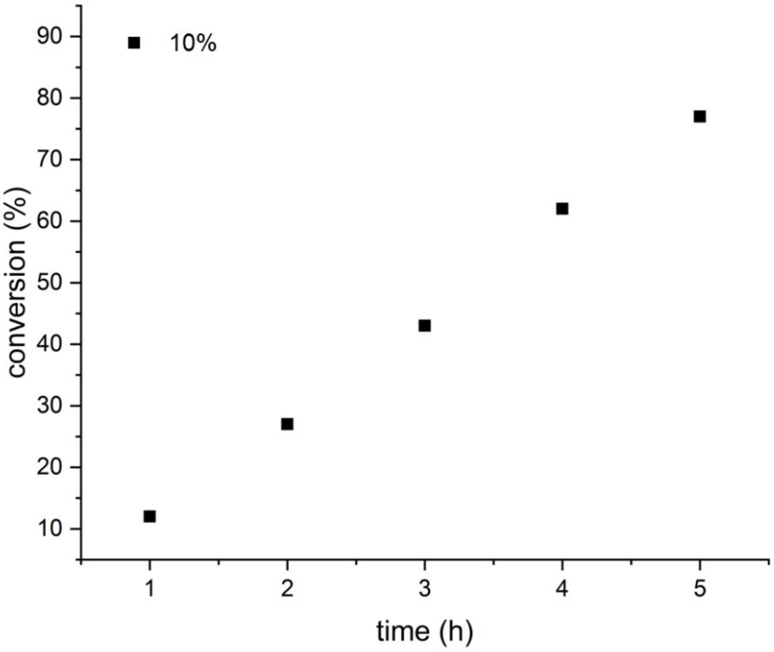

Figure S47. Conversion curves for cage **1**-catalysed isochroman oxidation reaction over 5 hours (with catalyst loading of 10% and a substrate concentration of 0.008 M, under 24 W 365 nm LEDs).

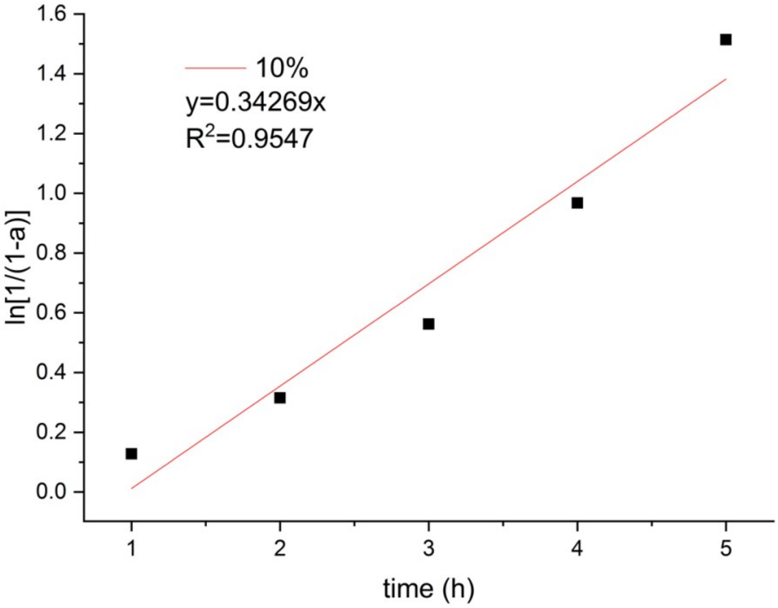

Figure S48. First-order kinetic plot of cage **1**-catalysed isochroman oxidation reaction over 5 hours (with catalyst loading of 10% and a substrate concentration of 0.008 M, under 24 W 365 nm LEDs).

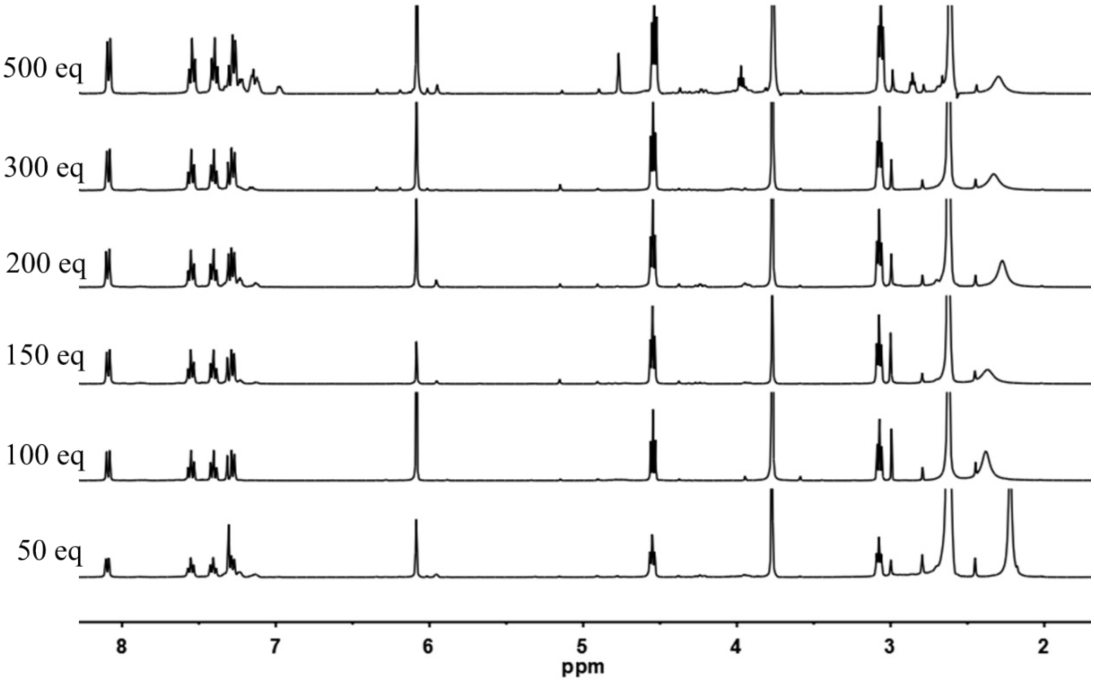

Figure S49 ^{1}H NMR spectrum (400 MHz, $CDCl_3$, 298 K) of photooxidation product of isochroman (50-500 equiv.) with the catalysis of cage **1**. 1,3,5- trimethoxybenzene was used as internal standard.

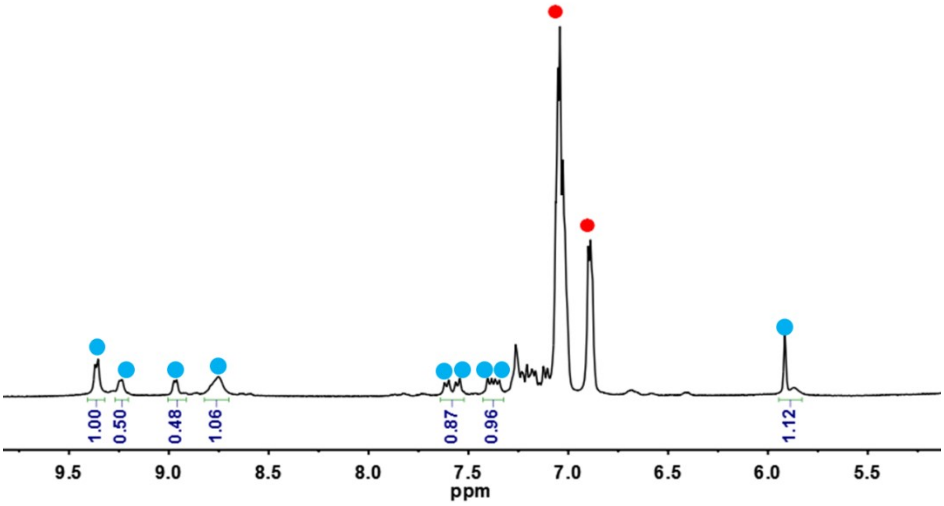

Figure S50. ^{1}H NMR spectrum (400 Hz, D_2O/DMSO-d_6, v/v = 4/1, 298 K) of cage **1** with 100 equiv. of isochroman. Integration radio indicates a 90% ratio of host-guest complex based on the methylene proton signal (H_e).

NMR titration and Calculation of K_a. The binding constant of cage **1** for isochroman and isochromanone have been estimated by ^{1}H NMR titrations and fitted with a Hill function. [S7-9]

$$log\frac{\theta_i}{1-\theta_i} = nlog[G] + nlog[K_a]$$

θ = saturated ratio
$\theta_i = \Delta\delta_i / \Delta\delta_{max}$ (for NMR titration)
n = Hill coefficient
[G] = concentration of guest
K_a = apparent association constant.

Where θ is the fraction of binding sites occupied by the guest, [G] is the guest concentration, n is the Hill coefficient describing cooperativity, and K_a is the apparent association constant. The Hill coefficient n describes the cooperative binding, where $n > 1$ indicates positive cooperativity, $n < 1$ indicates negative cooperativity, and $n = 1$ indicates no cooperativity.

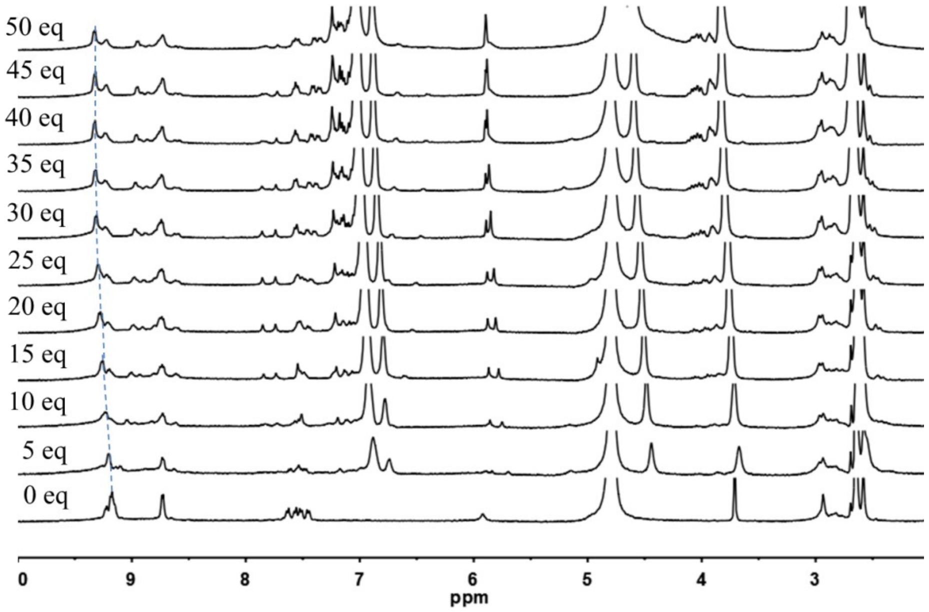

Figure S51. ^{1}H NMR titration (400 MHz, D_2O/DMSO-d_6, v/v = 4/1, 298 K) of cage **1** with isochroman.

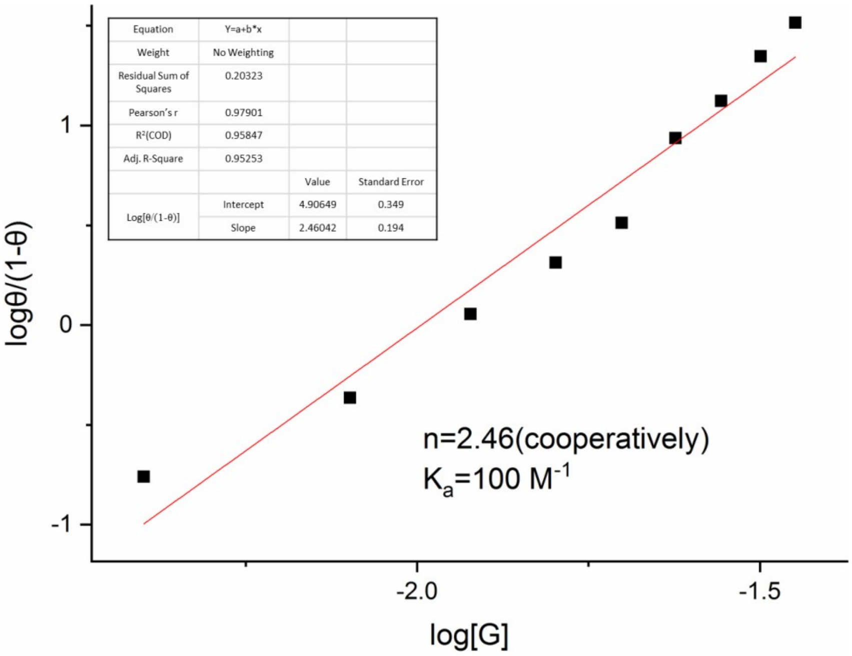

Equation	Y=a+b*x		
Weight	No Weighting		
Residual Sum of Squares	0.20323		
Pearson's r	0.97901		
R²(COD)	0.95847		
Adj. R-Square	0.95253		
		Value	Standard Error
Log[θ/(1-θ)]	Intercept	4.90649	0.349
	Slope	2.46042	0.194

Figure S52. Titration curve fitting with Hill function for cage **1** and isochroman. The apparent binding constant was determined to be 100 M^{-1}.

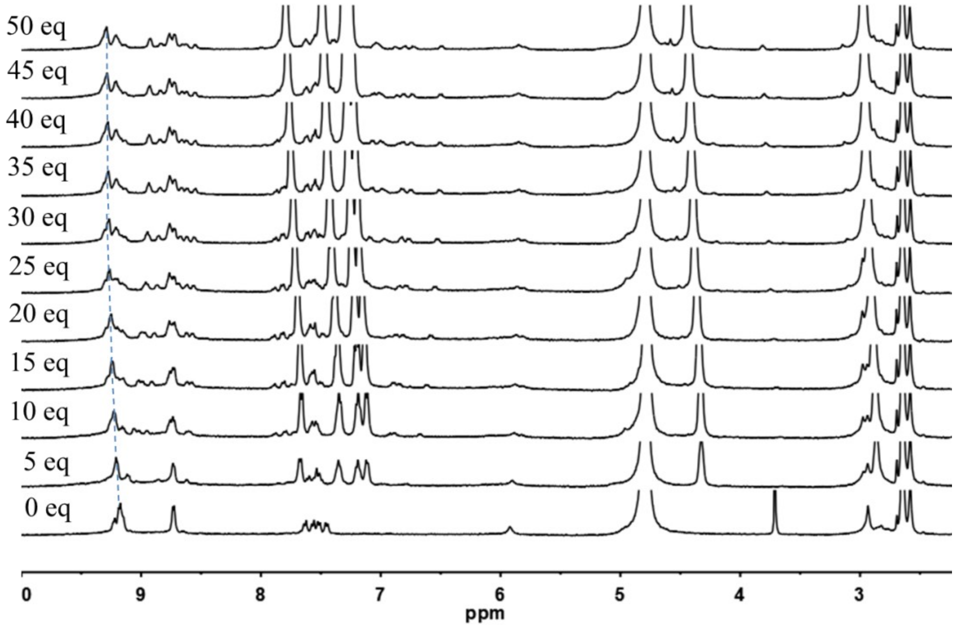

Figure S53 ^1H NMR titration (400 MHz, D_2O/DMSO-d_6, v/v = 4/1, 298 K) of cage **1** with isochromanone.

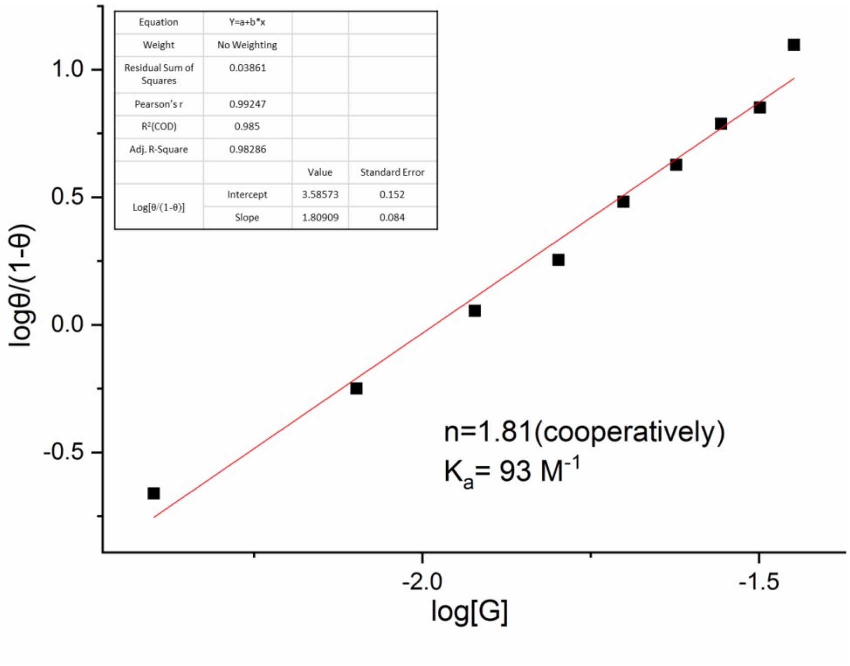

Equation	Y=a+b*x		
Weight	No Weighting		
Residual Sum of Squares	0.03861		
Pearson's r	0.99247		
R^2(COD)	0.985		
Adj. R-Square	0.98286		
		Value	Standard Error
Log[θ/(1-θ)]	Intercept	3.58573	0.152
	Slope	1.80909	0.084

Figure S54 Titration curve fitting with Hill function for cage **1** and isochromanone. The apparent binding constant was determined to be 93 M^{-1}.

5.2 Control experiments and proposed mechanism

Table S1 Control experiments for the photooxidation of isochroman. [a]

Entry	Varied condition	Conversion% (Yield%)[b]
1[d]	**1**	74 (50)
2[c]	none	n.d.
3[c]	N_2 instead of O_2	trace
4[c]	Without light	trace
5[d]	en-Pd$(NO_3)_2$	5 (3)
6[d]	**L** $(BF_4)_2$	39 (19)
7[d]	en-Pd$(NO_3)_2$+**L**	44 (21)

[a] Reaction conditions: substrates (0.07 mmol, 100 equiv.) and catalysts (1 equiv.) in 0.8 mL of H_2O/CH_3CN (v/v = 2/1) were irradiated under purple light (365 nm, 24 W) with stirring at room temperature. The products were then extracted with $CHCl_3$ without further purification. [b] Yields were determined by ^1H NMR with 1,3,5-trimethoxybenzene as the internal standard. [c] The reaction lasted 16 hours. [d] The reaction lasted 5 hours.

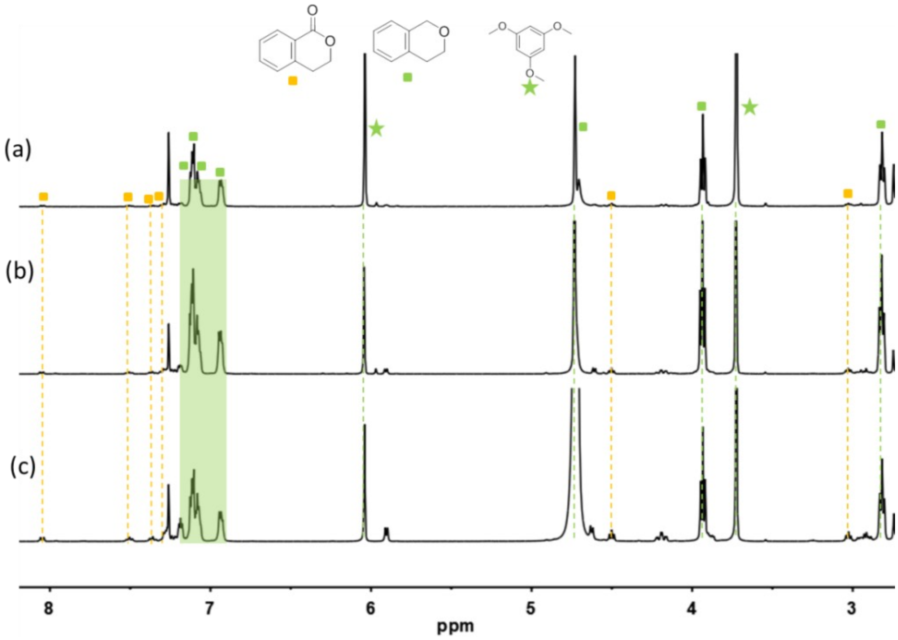

Figure S55. ^{1}H NMR spectra (400 MHz, $CDCl_3$, 298 K) of photooxidation products (yellow dots) of isochroman (green dots): a) without catalyst, b) with no light (24 W), c) under an atmosphere of N_2, corresponding to entry 2-4 in table S1. 1,3,5-trimethoxybenzene was used as internal standard (green pentagram).

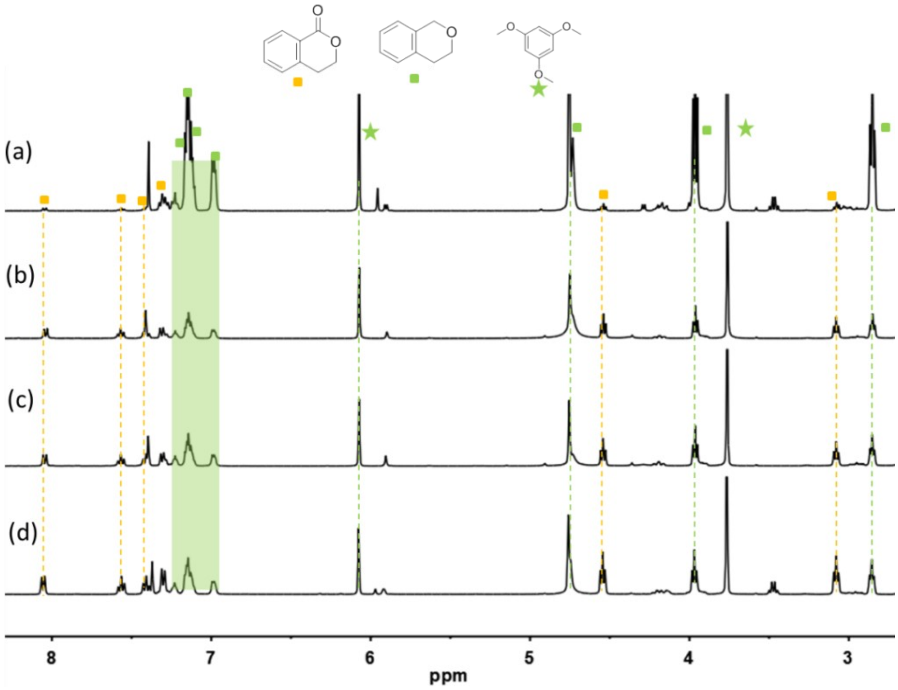

Figure S56. ^{1}H NMR spectra (400 MHz, $CDCl_3$, 298 K) of photooxidation products (yellow dots) of isochroman (green dots): a) using enPd$(NO_3)_2$, b) using L·$(BF_4)_2$, (c) using ligand **L** and en-Pd$(NO_3)_2$ in a 2:1 molar ratio, (d) using cage **1** as catalysts for 5 hours, corresponding to entry 1, 5-7 in table S1. 1,3,5- trimethoxybenzene was used as internal standard (green pentagram).

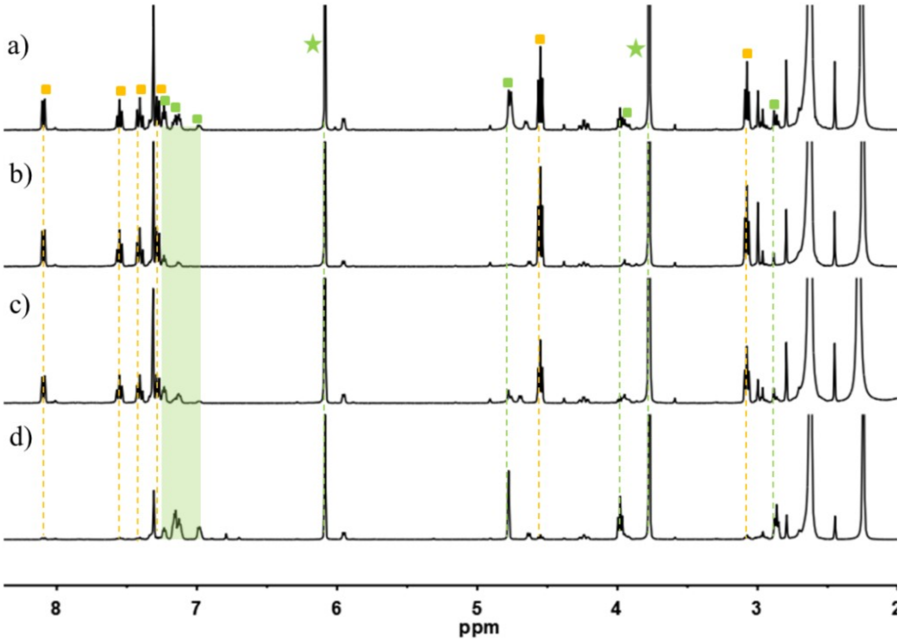

Figure S57. ^{1}H NMR spectra (400 MHz, $CDCl_3$, 298 K) of photooxidation product (yellow dots) of isochroman (green dots) with addition of different quenchers including a) $AgNO_3$ (electron quencher), b) NaN_3 ($^1O_2$ quencher), c) t-butanol ($^{\bullet}OH$ quencher), and d) benzoquinone ($O_2^{\bullet -}$ quencher). 1,3,5-trimethoxybenzene was used as internal standard (green pentagram).

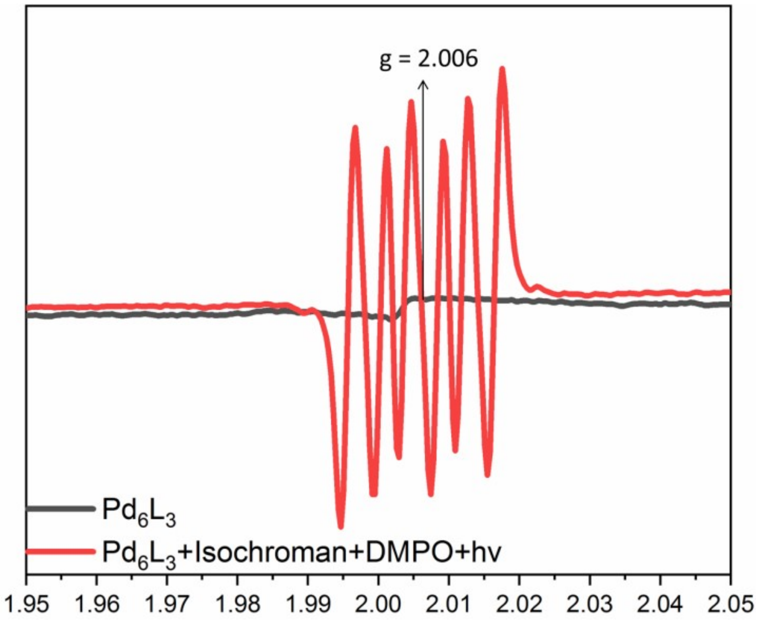

Figure S58. ESR spectra of cage **1** in H_2O/DMSO (v/v = 4/1) solution before (black line) irradiation at 100 K under N_2, and ESR spectrum of the mixtures of 100 equivalents of isochroman and cage **1** in the presence of DMPO in MeOH solution after (red line) irradiation (xenon lamp; 200 mW/cm^2) at r.t..

LUMO and HOMO calculation. The optical band gap (E_g) of cage 1 is 3.31 eV according to the Kubelka–Munk equation (Equation 1) (Figure S59). Where α, h, ν and A represent the absorption factor, Planck's constant, optical frequency and optical absorption constant.

$$(\alpha h v) = A(hv - E_g)^{n/2} \qquad (1)$$

$$E_{LUMO} =- [E_{red} + 4.8 - E_{(Fc/Fc^+)}] \text{eV} \qquad (2)$$

$$E_g = E_{LUMO} - E_{HOMO} \qquad (3)$$

Using the F_c/F_c^+ coupling potential as the reference electrode, LUMO energy level of cage **1** can be calculated from the first reduction potential of the cage (-0.320 V) according to Equation 2.[S10-12] Finally, the respective HOMO energy level can be determined according to Equation 3.

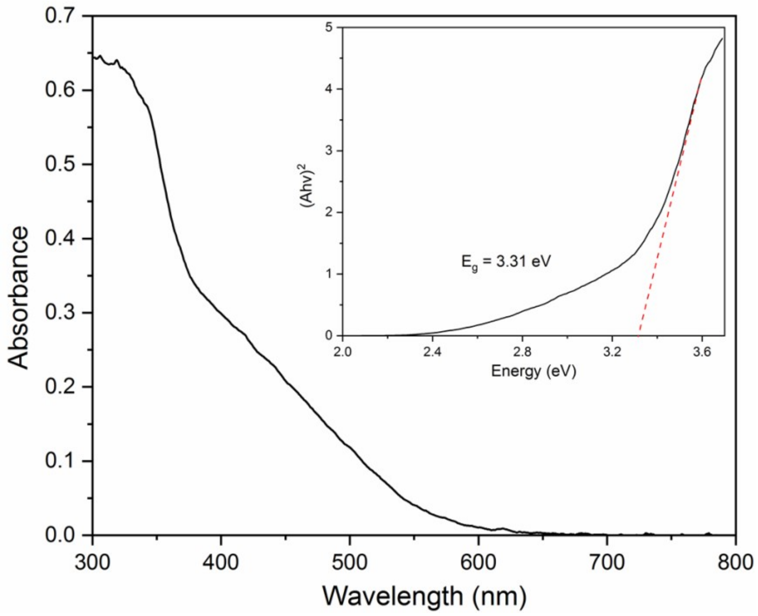

Figure S59. Solid UV-Vis spectrum of cage **1** with inset showing Tauc plot diagram.

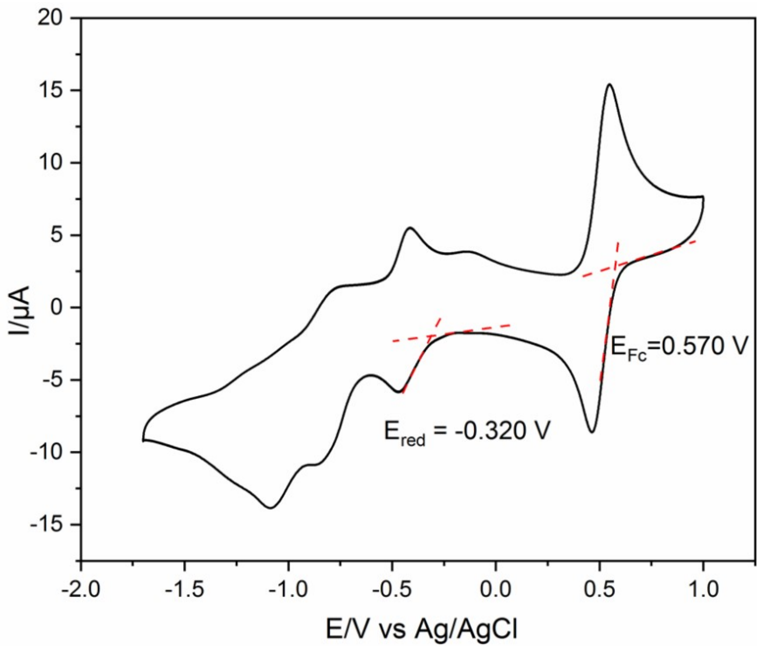

Figure S60. CV of ferrocene-cage (0.17 mM) in Bu_4NPF_6 (0.1 M) DMSO solution at a scan rate of 0.1 V/s.

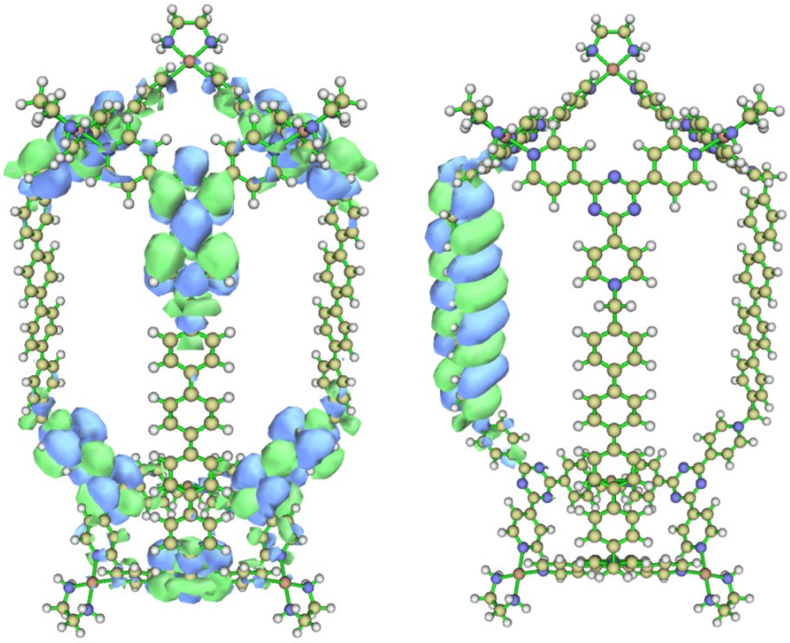

LUMO HOMO

Figure S61. a) LUMO (left) and HOMO (right) orbitals distribution in cage **1** from DFT calculation. Computational detail: The structure optimization of the cage was performed by the GFN1-xTB. In the calculation, only the positions of the H atoms in the crystal structure were optimized. Molecular orbitals (HOMO and LUMO) of the cage were calculated at B3LYP/6-31G(d)/SDD level. The IEFPCM solvation model was employed to consider the solvent effect (water).[S13-14]

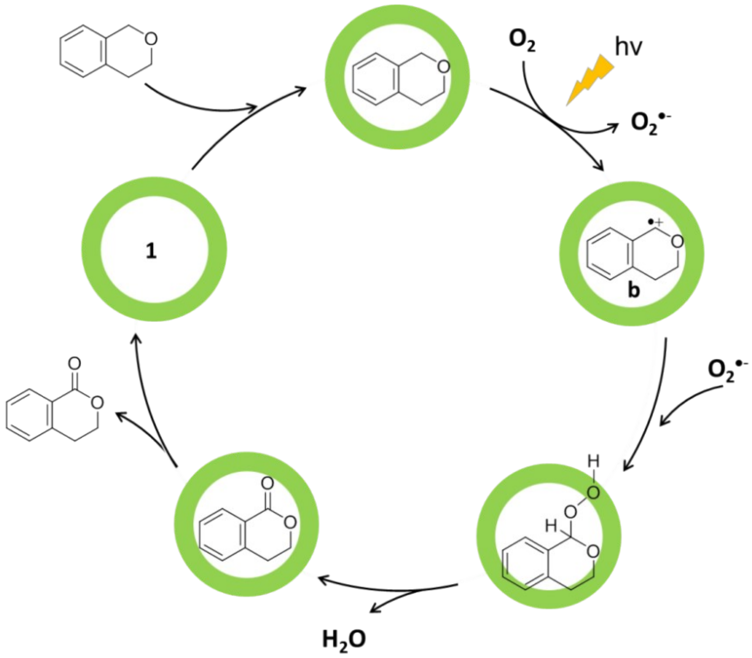

Figure S62. Proposed mechanism for possible photocatalytic process.

6. Supplementary references

S1. H.L., Anderson; S., Anderson; J.K.M., Sanders. *J. Chem. Soc. Perkin. Trans.*, 1995, 2231–2245.

S2. W. Chen, J. R. Widawsky, H. Vázquez, S. T. Schneebeli, M. S. Hybertsen, R. Breslow and L. Venkataraman, *J. Am. Chem. Soc.*, 2011, **133**, 17160-17163.

S3 V. D. Nguyen, C. A. McCormick, F. A. Vaccaro, K. E. Riley, C. J. Stephenson, J. T. Mague and L. V. Koplitz, *Polyhedron*, 2016, **114**, 428-434.

S4. Sheldrick G. M., A short history of SHELX, *Acta Crystallogr. Sect. A*, 2008, 64(1): 112.

S5. Spek A. L., Single-crystal structure validation with the program PLATON. J. *Appl. Crystallogr.*, 2003, 36(1): 7.

S6. Voss N. R.; Gerstein M., 3V: cavity, channel and cleft volume calculator and extractor. *Nucleic. Acids. Res.*, 2010, 38(Web Server): W555.

S7. D. Yang, J. L. Greenfield, T. K. Ronson, L. K. S. von Krbek, L. Yu and J. R. Nitschke, *J. Am. Chem. Soc.*, 2020, **142**, 19856-19861.

S8. H. Takezawa, T. Murase, G. Resnati, P. Metrangolo and M. Fujita, *J. Am. Chem. Soc.*, 2014, **136**, 1786-1788.

S9. K. Li, K. Wu, Y.-L. Lu, J. Guo, P. Hu and C.-Y. Su, *Angew. Chem. Int. Ed.*, 2022, **61**, e202114070.

S10. L. Yang, J. Yuan, G. Wang, Q. Cao, C. Zhang, M. Li, J. Shao, Y. Xu, H. Li and J. Lu, *Adv. Funct. Mater.*, 2023, **33**, 2300954.

S11. Y.-L. Dong, Z.-Y. Jing, Q.-J. Wu, Z.-A. Chen, Y.-B. Huang and R. Cao, *J.*

Mater. Chem. A, 2023, **11**, 8739-8746.

S12. S. O. Jung, Q. Zhao, J.-W. Park, S. O. Kim, Y.-H. Kim, H.-Y. Oh, J. Kim, S.-K. Kwon and Y. Kang, *Org. Electron.*, 2009, **10**, 1066-1073.

S13. T. Lu and F. Chen, *J. Comput. Chem.*, 2012, 33(5): 580-592.

S14. T. Lu, *J. Chem. Phys.*, 2024, 161(8): 082503.